B cell metabolic screening in primary antibody-deficiency identifies succination as an inflammatory immuno-metabolic pathology

---

Inauguraldissertation

zur

Erlangung der Würde eines Doktors der Philosophie

vorgelegt der
Philosophisch-Naturwissenschaftlichen Fakultät
der Universität Basel

von

Anne-Valérie Burgener

aus Saas- Fee, Wallis

Basel, 2019

Genehmigt von der Philosophischen-Naturwissenschaftlichen Fakultät

auf Antrag von

Prof. Dr. Christoph Hess
Prof. Dr. Jean Pieters

Basel, den 24. April 2018

Prof. Dr. Martin Spiess
Dekan

Table of contents

ACKNOWLEDGEMENTS

The PhD study has been a time of great pleasure, new challenges and intense learning, not only in the scientific area, but also on a personal level. Here, I would like to give credits to the persons who have supported and helped me trough this journey.

First and foremost, I would like to give my sincere thanks to my mentor Christoph Hess for the continuous support of my PhD study and research, for his huge encouragement and his wise counsel. I always appreciated his open door, his fantastic ideas and his constructive criticism. Without his guidance and his driving force trough this entire process this PhD would not have been achievable.

In my daily work, I have been surrounded by a great team. My sincere thanks goes to all present and former lab mates, Rebekah Steiner, Gunhild Unterstab, Patrick Gubser, Bojana Durovic-Müller, Maria Balmer, Layla Develioglu, Raja Epple, Tamara Kellerhals, Yannic Lecoultre, Philipp Dehio, Sarah Dimeloe, Marco Fischer and Gideon Hönger. Particular I would like to thank Jasmin Grählert, Jonas Lötscher and Jordan Löliger for their friendship and their great support also during difficult times. I would like to thank Glenn Bantug for the assistance and advice for my project. Special thanks goes also to Olivier Bignucolo for the construction of the amazing structure model.

I greatly appreciate the supervision and teaching of Mike Recher during my clinical work and his constructive feedback on the scientific part. Many thanks also to Benedikt Meyer for his great help with experiments.

I would like to give my credits to Matthias Mehling. He provided me with the basic tools needed for my research study.

Further, I would like to express my gratitude to Rebecca Higgins and Alexander Navarini. Their excellent collaboration made an important contribution to this work.

My sincere thanks goes to Michel Enamorado, Sarai Martinez-Cano and David Sancho from the Immunobiology lab in Madrid. I greatly appreciate the support, the scientific discussions and the unique opportunity to work in Madrid.

I am grateful to all of those with whom I have had the pleasure to collaborate during this project. In particular I wish to thank to Eric Ma and Russel Jones for the tracing studies, Ursula Sauder

for the beautiful electron microscopy pictures and Robert Ivanek for his help with RNA seq analyses. Further I would like to express my thanks to Nathan Cantoni and Christian Kahlert for collaboration on the clinical side. Finally a special thanks goes to all the patients contributing to a significant part of this project.

I would further like to acknowledge the members of my thesis committee Christoph Hess, Mike Recher, Prof. Jean Pieters and Prof. Manuel Battegay for valuable advice and their willingness to review this thesis.

Most importantly, I would like to express my deepest gratitude to Claudio Gasser, my parents Caroline and Roland Burgener and my sisters Maya Burgener and Daria Widmer, it would not have been possible without their love, endless support and continued patience.

SUMMARY

Cellular metabolic pathway usage and immune cell function are intimately interlinked. Whether screening metabolic activity of defined immune cell subsets has clinical value, or is effective in guiding discovery of molecular immune pathology, has not been previously explored.

Here we prospectively screened glycolysis (extracellular acidification rates – ECAR) and mitochondrial respiration (oxygen consumption rates – OCR) in B cells of healthy subjects (n=15) and patients with primary antibody deficiency (PAD, n = 14). Mean ECAR values were similar in both cohorts, whereas – counterintuitively – mean OCR values were *higher* in PAD patients. The highest OCR values grouped three study participants with primary polyclonal B cell lymphocytosis (PPBL), a condition characterized by expansion of marginal zone (MZ)-like B cells. Guided by this B cell hyper-respiration phenotype, whole exome sequencing identified rare germline mutations in subunit A of the succinate dehydrogenase (SDHA) gene in these three patients. Functional assays pinpointed SDHA *gain-of-function* driving fumarate accumulation, which increased succination of several proteins – including KEAP1. Succination of KEAP1 promotes accumulation of the transcription factor Nrf-2, and inhibition of Nrf-2 established that the inflammatory output of MZ-like B cells from PPBL patients was Nrf-2 dependent.

Our study identifies pathologic retrograde signaling as a novel mechanism underlying immune dysregulation in PAD. Specifically, in MZ-like B cells of the PPBL patients enrolled in this study, SDHA-driven accumulation of fumarate engaged retrograde signaling via KEAP1–Nrf-2 to drive transcription of inflammatory cytokines. OCR screening of a clinically justified cell population thus helped to uncover a novel molecular disease mechanisms and pinpointed new therapeutic targets.

INTRODUCTION

Primary immunodeficiency disorders (PIDs) are rare genetic syndromes that arise from defects in the immune system. More than 350 PID entities have been defined to date [1]. The most common symptomatic adult PID is primary antibody deficiency (PAD) – ranging from complete absence of antibodies to immunoglobulin subclass deficiency [2,3]. PADs are often due to B cell intrinsic defects, yet causes and genetics of PADs are complex and only in a minority of cases pathogenic mutations have been identified (e.g. mutations in the genes encoding for Bruton tyrosine kinase, B cell activating factor, or CD19) [3-10].

PADs can present with a spectrum of clinical problems, ranging from infections only (approx. 50% of PAD patients), to autoinflammation, autoimmunity, lymphoproliferation and allergy.

Infectious complications are predominantly characterized by prolonged, recurrent bacterial infections of the respiratory- and also gastrointestinal tract [2,11]. Persistent infections support the pathogenesis of inflammation and autoimmunity. Mechanistically, during an acute infection immune cells rapidly proliferate in order to clear the pathogen and subsequently undergo apoptosis to return to steady state. High burden of apoptotic cell debris triggers formation of autoantibodies and accumulation of immune complexes, both driver of autoinflammation [12-14]. A broad spectrum of autoimmune disorders is present in PADs varying from rheumatic arthritis, vasculitis, autoimmune haemolytic anaemia, immune thrombocytopenia, glomerulonephritis, inflammatory bowel disease and also dermatologic disorders as vitiligo or psoriasis [14,15].

Lymphoproliferation as lymphadenopathy, splenomegaly and also lymphomas is another frequent complication in PADs [16,17]. In addition of defective DNA repair mechanism and viral infections as EBV and HHV8, also chronic inflammatory processes contribute to the development of lymphomas [18,19]. In particular the inflammatory cytokine IL-6, the major stimulus of the synthesis of the acute phase protein CRP, promotes B cell proliferation and differentiation and is a growth factor for malignant B cells [20-22]. In deed it has been reported that IL-6 supports virus related lymphoproliferation and patients with lymphomas and high IL-6 serum concentration have been associated with poorer survival rates [23].

Susceptibility to infection is prevented by substitution of immunoglobulins. By contrast, non-infectious complications are not affected by immunoglobulin replacement therapy, and contribute to excess mortality in these patients [24].

Over the last years our understanding of how cellular metabolism governs immune cell function has rapidly increased [25-28]. Specifically, various facets of glycolysis have been demonstrated to impact the function of many immune cell types, including B cells [29-31]. Glutamine metabolism – critically required for effector T cell-, NK cell-, macrophage- and DC function – is also increased in activated B cells [31-34]. Glutaminolysis can importantly contribute to ATP production, and glutamine-derived α-ketoglutarate (α-KG) serves as anaplerotic source of tricarboxylic acid (TCA) metabolites [32,33,35]. The TCA cycle operates tightly integrated with the respiratory chain within mitochondria [36,37]. The respiratory chain complex II, known as succinate dehydrogenase (SDH), forms the physical link between the TCA and the mitochondria respiratory chain. SDH contains four subunits SDHA, SDHB, SDHC and SDHD. SDHA, the major catalytic domain, oxidizes the TCA substrate succinate to fumarate and transfers generated electrons to its subunits [38,39].

To facilitate more efficient transfer of electrons, the mitochondria respiratory complexes are organized in larger supramolecular structures. The formation of supercomplexes allows higher stability and consequently leads to increased activity [40].

Fueled by glycolysis, glutaminolysis or β-oxidation (i.e. lipid oxidation), mitochondrial oxidative phosphorylation (OxPhos) is producing most of the ATP required for anabolic processes, including cell proliferation or production of effector molecules secreted by immune cells [41-43].

Importantly, several non-bioenergetic features of mitochondria further critically regulate immune cell function. For example, in LPS-stimulated macrophages accumulation of the TCA intermediate, succinate, promotes transcription of inflammatory genes by driving mitochondrial hyperpolarization and mitochondrial reactive oxygen species (mROS) dependent HIF-1α stabilization [44]. In $CD4^+$ T cells, production of mROS has been linked to the activation of NFAT and production of IL-2, in B cells to reduced expression of CD19 and inhibition of signaling through the B cell receptor (BCR) [45,46]. In nascent activated memory $CD8^+$ T cells, mitochondrial function and epigenetic remodeling have been shown to be interlinked via pyruvate oxidation and conversion of pyruvate-derived citrate to acetyl-CoA – which is required for histone acetylation [47,48]. Metabolites of the TCA cycle can also directly activate (α-KG), or inhibit (fumarate, succinate) dioxygenases that are involved in histone and DNA demethylation, thus modulating transcriptional activity [49,50]. Indeed, the ratio of α-KG to [fumarate & succinate] has been shown to govern epigenetic changes and transcriptional programs in macrophages [51,52].

Protein succination – the fumarate-dependent, non-enzymatic addition of a succinyl-group to thiol-groups in proteins – provides another emerging link between mitochondrial function, i.e. fumarate production, and the transcriptional activity of cells [53,54]. Loss of function mutation of fumarase hydratase (FH) has been associated with decreased mitochondria respiration and accumulation of fumarate, which has been suggested to post-translational modify kelch-like ECH associated protein 1 (KEAP1) via succination. Inhibition of KEAP1 activates transcription factor nuclear factor, erythroid 2 like 2 (Nrf-2) a regulator of inflammation and antioxidant response [55,56]. In theory a gain of function mutation in the SDHA gene could also impact transcriptional activity via succination by increasing endogenous fumarate levels. Remarkably SDH gain of function mutation has not yet been described, while SDH loss of function mutations are well characterized and interlinked with various diseases affecting tissues with high energy demands [57].

In macrophages and T cells, pharmacologically increasing fumarate levels has recently been shown to drive succination events, and oxidative stress in type 2-diabetes has been described to lead to protein succination. In each of these scenarios succination was demonstrated to alter protein-, and thus cellular functions [55,58,59].

Also numerous mutations in genes of TCA enzymes, mitochondria respiratory chain complexes and metabolic check point kinases have impact on cellular functions [60-62]. Mutations in mitochondrial respiratory complexes have been linked with neurological disorders, cardiopathy and lactic acidosis [61,63-65].

Mutations in the isozymes isocitrate dehydrogenase (*IDH*) in cancers drive accumulation of the α-KG analog (*R*)-2-hydroxyglutarate (R-2-HG), which inhibits ATP synthase of T cells. This leads to inhibition of T-cell receptor (TCR) signalling and subsequently to impaired activation and proliferation [66].

Gain of function mutation in Pi(3)k–mTOR axis a key molecular regulator of the metabolic pathway, results in increased glucose metabolism, cell growth and proliferation and promote lymphocyte senescence and immunodeficiency [67,68].

In my thesis, I explored the idea that metabolic pathway activity of B cells in patients – or subgroups of patients – with antibody deficiency may be deregulated, and that such deregulated cellular metabolism could contribute to disease. To test this concept, we *(i)* screened, directly *ex vivo*, the activity of glycolysis and mitochondrial respiration among B cells from healthy

individuals and patients with PAD, and *(ii)* investigated, in a subset of patients, how cellular metabolism and B cell immuno-pathology interrelated at the molecular level.

RESULTS

B cells from patients with primary antibody deficiency have increased oxygen consumption rates.

First, to establish normal values for bulk B cell oxygen consumption (oxygen consumption rates – OCR) and glycolysis (extracellular acidification rates – ECAR), we measured both these parameters in B cells from healthy individuals (n = 15) using a metabolic flux analyzer (**Fig. 1A**). Normal values were then compared with those obtained in patients with PAD (n = 14) (**Fig. 1A**). Antibody deficient patients were prospectively included in the study (inclusion criteria: age ≥ 18y; total immunoglobulin (Ig) G level < 7g/L, or subclass deficiency (defined as IgG_1< 4.9 g/L, IgG_2 <1.5 g/L, IgG_3<0.2 g/L or IgG_4< 0.08 g/L); no evidence for secondary antibody deficiency) and metabolic screening experiments were performed blinded for clinical information. This prospective screening approach identified higher mean respiratory activity (OCR) in B cells from patients as compared to the healthy control population. Glycolysis, by contrast, was similar in patients and controls (**Fig. 1A**). Distribution of age was comparable between patients and controls, and in either cohort no strong age dependence of OCR or ECAR was observed (**Fig. S1A**). Also, no difference in OCR or ECAR was detected between female- and male study participants, and between CMV^+ and CMV^- individuals (**Fig. S1B**). Three patients with a particularly high OCR stood out from this analysis (Patients #1, #8, and #9). Intriguingly, these 3 non-related patients were diagnosed with the same disease, namely *Peripheral Polyclonal B Cell Lymphocytosis* (PPBL). PPBL is a rare disorder, originally described by Gordon *et al.* in 1982 [69], characterized by expansion of B cells with a marginal zone-like phenotype ($CD19^+$ $CD27^+$ IgD^+), bi-nucleated lymphocytes, elevated levels of serum IgM and – the inclusion criterion for this study – low levels of IgG. The etiology of PPBL is not known, yet a genetic basis has been suggested [70,71]. PPBL is often clinically silent or oligosymptomatic, yet it may also present with signs and symptoms of severe immune dysregulation and it can evolve toward clonal proliferation or overt malignant lymphoma [72,73]. The three PPBL patients included in this study all had clinically manifest disease, specifically one or several of the following: bronchitis (n = 3), splenomegaly (n = 2), arthralgia (n = 1), weight loss (n = 1), fatigue (n = 1), large and small vessel vasculitis, scleritis, tendinitis, perichondritis (n = 1). Clinical and immunologic characteristics of all PAD patients, including the PPBL patients, are summarized in **Table 1A** and **B**, respectively. From the PPBL patient with the most severe disease course (Patient #9), **Figure 1B** is providing a summary of C-reactive protein (CRP) values over time and associated disease

signs and symptoms; an example of an episode with cutaneous small-vessel vasculitis (leukocytoclastic vasculitis), and a CT scan demonstrating periaortitis. In **Figure 1C** a representative example of the relative distribution of IgD vs. CD27 expressing $CD19^+$ lymphocytes (i.e. B cells) is shown from a healthy control and one PPBL patient (Patient #8). All three patients with PPBL included in this study had almost exclusively peripheral blood B cells with a marginal zone-like phenotype. For comparison, an example of flow-sorted marginal zone-like B cells (i.e. IgD^+ $CD27^+$ $CD19^+$ lymphocytes) is also shown (**Fig. 1C**). To test whether increased respiration was a general feature of marginal zone-like B cells, we compared the OCR of PPBL B cells with that from sorted marginal zone-like B cells of healthy individuals. The OCR of marginal zone-like B cells from healthy individuals was similar (or if anything somewhat lower) when compared to that of bulk B cells (**Fig. 1D**, upper left panel). Next, temporal stability of hyper-respiration was determined by re-assessing the OCR 12 months after baseline measurements. No change in the respiratory phenotype was observed, establishing its robustness over time (**Fig. 1D**, lower left panel). Hyper-respiration of PPBL B cells was also unaffected by *in vivo* exposure to a rapalogue (sirolimus) (**Fig. 1E**), which was used in Patient #9 in an (unsuccessful) attempt to control large vessel vasculitis – further pointing to a distinct stability of this metabolic phenotype. In contrast to mitochondrial respiration, basal glycolysis (ECAR) was similar in PPBL patients and healthy controls, and also not different between marginal zone-like- and bulk B cell populations (**Fig. 1D**, upper right panel). Alike respiration, glycolysis – although being somewhat more variable than OCR – was stable over time (**Fig. 1D**, lower right panel). In both, healthy- and PPBL B cells, glycolysis similarly increased when pharmacologically shutting down mitochondrial respiration (data not shown), as well as when stimulating B cells with IL-21 and CD40L (**Fig. 1F**). Lastly, also glucose uptake was not consistently different between healthy- and PPBL B cells (**Fig. 1G**). Of note, relative distribution of T cell subpopulations was similar in healthy controls and PPBL patients (**Fig. S1C**). Further, bulk T cells from PPBL patients did not differ in both OCR and ECAR values from healthy control cells (**Fig. S1D**). Together these data identified hyper-respiration, at the cohort level, as an immunometabolic trait of primary bulk B cells in patients with PAD. In the three study participants with the highest OCR, hyper-respiration was a stable feature of expanded marginal zone-like B cells – which were representing as much as 90% of their peripheral B cell pool (= PPBL-typic).

Figure 1

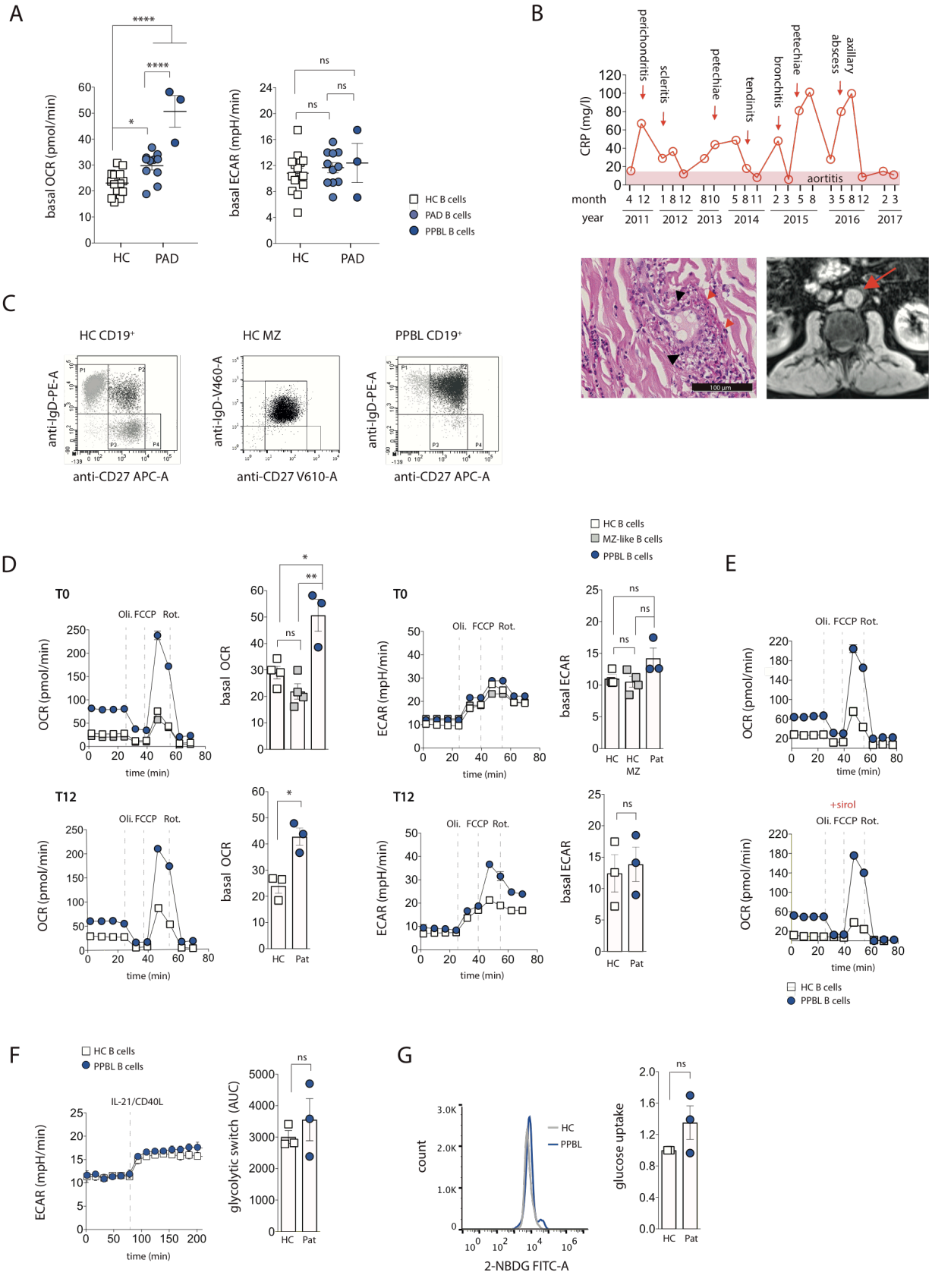
A
basal OCR (pmol/min)
basal ECAR (mpH/min)
HC
PAD
HC B cells
PAD B cells
PPBL B cells
B
CRP (mg/l)
perichondritis
scleritis
petechiae
tendinits
bronchitis
petechiae
abscess
axillary
aortitis
month
year
C
HC CD19+
HC MZ
PPBL CD19+
anti-IgD-PE-A
anti-IgD-V460-A
anti-CD27 APC-A
anti-CD27 V610-A
D
T0
T12
Oli. FCCP Rot.
OCR (pmol/min)
ECAR (mpH/min)
basal OCR
basal ECAR
time (min)
HC B cells
MZ-like B cells
PPBL B cells
E
+sirol
F
IL-21/CD40L
glycolytic switch (AUC)
G
count
2-NBDG FITC-A
glucose uptake

Figure 1: Metabolic profile of healthy controls and patients with primary antibody deficiency.

(**A**) Basal mitochondrial respiration (oxygen consumption rate – OCR) (*left panel*) and basal glycolysis (extracellular acidification rate – ECAR) (*right panel*) of B cells from healthy controls (HCs) (n = 15) and patients with primary antibody deficiency (PAD) (n = 14). Patients (n = 3) with persistent polyclonal B cell lymphocytosis (PPBL) had the highest OCR values.

(**B**) *Upper panel:* C-reactive protein (CRP) measurements over time (red line) and clinical symptoms (red arrows) from Patient #9. *Lower panel:* Left, histopathology of a skin biopsy, depicting leukocytoclastic vasculitis (perivascular neutrophilic infiltration and nuclear debris (black arrowheads), and deposition of fibrin (red arrowheads)). Scale bar, 100 μm. Right, abdominal CT scan showing a contrast enhanced soft-tissue dense area (red arrow) around the aorta, reflecting periaortitis.

(**C**) Representative flow cytometry dot blots showing the distribution of $CD19^+$ B cells expressing IgD vs. CD27 among a HC, sorted marginal zone (MZ)-like B cells from a HC, and a PPBL patient.

(**D**) Representative baseline OCR and ECAR measurements (T0) of primary B cells or primary MZ-like B cells from HCs, and primary B cells from a PPBL patient. Shown are basal values and measurements following mitochondrial perturbation with oligomycin (Oli.), FCCP, and rotenone (Rot.). Summary bar graphs represent basal respiration (OCR) and basal glycolysis (ECAR) of primary B cells (n = 4), primary MZ-like B cells (n = 4) from HCs, and primary B cells from PPBL patients (n = 3). *Lower panels:* Follow-up one year after baseline assessment (= T12), showing representative OCR and ECAR measurements of primary B cells from a HC and primary B cells from a PPBL patient. Mitochondrial perturbation was performed as above. Summary bar graphs represent T12 basal respiration (OCR) and T12 basal glycolysis (ECAR) of primary B cells from HCs (n = 3), and primary B cells from PPBL patients (n = 3).

(**E**) Mitochondrial perturbation profiles of primary B cells from a HC, and from PPBL Patient #9 before (*upper panel*) and during sirolimus (2 mg) treatment of the patient (*lower panel* – treatment duration at the time of analysis: 2.5 months).

(**F**) Representative ECAR measurements of primary B cells from a HC and a PPBL patient before and following injection of IL-21 plus CD40L directly into the metabolic flux analyzer (dashed line). The bar graph summarizes glycolytic switching, calculated as area under the curve (AUC) after activation of primary B cells from HCs (n = 3) and PPBL patients (n = 3).

(**G**) Representative flow cytometry histogram, reflecting glucose (2-NBDG) uptake of activated primary B cells from a HC and a PPBL patient. The bar graph summarizes glucose uptake calculated as geometric mean fluorescence (gMFI) of activated primary B cells from PPBL patients (n = 3) relative to that of HCs (n = 3). Cells were activated with IL-21 plus CD40L for 24 hours.

Data are represented as mean ± SEM. Statistical significance was assessed by one-way ANOVA (**A**), or unpaired t-test (**D-G**). *$p < 0.05$, ** $p < 0.01$, *** $p < 0.001$, **** $p < 0.0001$, ns, not significant. See also **Figure S1**.

Table 1

A

Pat	Sex	Age at dx (y)	Infection	Lymphoproliferation	Autoimmunity	Others
1	f	46	sinusitis, bronchitis	splenomegaly		athralgia
2	f	45	bronchitis, pneumonia	splenomegaly		athralgia
3	m	21	sinusitis, bronchitis pneumonia	splenomegaly retroperitoneal lymphadenopathy	vitiligo	
4	f	62	postinterventional wound infections			
5	m	58		splenomegaly, axilar lymphadenopathy	autoimmune thrombocytopenia	
6	m	30		splenomegaly	autoimmune hemolytic anaemia	
7	m	25	akne inversa, skin abscesses	splenomegaly	atopy	
8	f	51	otitis, sinusitis, bronchitis	splenomegaly		exanthema, fatigue, weight loss,
9	m	54	bronchitis		perichondritis, scleritis, tendinis, vascultis	
10	f	41	bronchitis, sinusitis, pneumonia	bilateral hilar lymphadenopathy		fatigue
11	f	35	bronchits, sinusitis		diabetes mellitus	
12	f	59	bronchits, pyelonephritis		psoriasis	
13	f	34			autoimmune keratitis	fatigue
14	f	59	bronchitis pneumonia	retroperitoneal lymphadenopathy	autoimmune thrombocytopenia	

B

	IgG g/L	IgM g/L	naive /µl $CD19^+ CD27^- IgD^+ IgM^+$	marginal zone-like /µl $CD19^+ CD27^+ IgD^+ IgM^+$	class switched /µl $CD19^+ CD27^+ IgD^- IgM^-$	CD21low /µl $CD19^+ CD21^{low} CD38^-$	transitional /µl $CD19^+ CD38^+ IgD^+ IgM^+$	plasmablasts /µl $CD19^+ CD38^{++} IgD^- IgM^-$
ref value	7-16	0.4-2.3	66-228	8-172	8-102	1-12	1-5	1-5
Pat								
1	5.9	9.04	225	2471	82	94	6	<3
2	IgG_4< 0.05	2.76	128	72	28	5	6	<1
3	0.9	0.22	143	28	<1	6	2	<1
4	5.8	2.19	87	33	16	4	4	1
5	3.4	0.45	150	99	4	8	6	<1
6	4.3	0.22	95	13	2	5	<1	<1
7	6.7	0.36	244	33	9.1	3	5	<1
8	4.4	4.47	554	2168	11	39	3	<3
9	5	7.75	276	455	28	71	9	5
10	2.85	0.24	332	32	5	6	11	<1
11	3.5	1.15	81	86	11	1	1	<1
12	3.6		289	74	16	3	10	<1
13	6.3	2.21	156	92	69	2	5	<1
14	1.6	1.47	170	3	<1	40	9	<1

Mitochondrial morphology and expression of respiratory chain proteins is normal in PPBL B cells.

Given the robustness of the hyper-respiration B cell phenotype among PPBL patients, we went on to analyze mitochondrial content and ultrastructure of primary PPBL B cells in comparison to primary B cells from healthy donors. No differences in ultrastructure were identified, with normal size, shape, cristae morphology, and matrix morphology of mitochondria in B cells from PPBL patients. Also when quantifying cell area; mitochondrial area; number of mitochondria per cell, and length over width (aspect ratios), mitochondria of B cells from PPBL patients appeared normal (**Fig. 2A**). We then probed for protein expression of components of each of the respiratory chains, specifically NDUFB8 (complex I), SDHB (complex II), UQCRC2 (complex III), COX II (complex IV), and ATP5A (complex V) in B cells from a healthy control and a patient. None of these proteins differed in abundance between primary PPBL B cells and B cells from healthy donor (**Fig. 2B**). To more comprehensively define whether either abundance of respiratory chain complexes, or super-complex formation differed between normal and PPBL B cells, blue native (BN)-PAGE immunoblot analyses were used. Due to limited availability of primary patient material these experiments were performed using enriched mitochondria from EBV-immortalized B cell lines. In both, healthy and PPBL B cell lines, expression levels of complexes I–V were similar. Also, formation of complex I containing super-complexes (I plus III, I plus III plus IV), and assembly of complex III plus IV was not different between both groups (**Fig. 2C**). Lastly, we also stained primary B cells from healthy donors and those from PPBL patients with the mitochondrial dyes, MTR and MTDR, which both accumulate dependent upon mitochondrial membrane potential. While mitochondrial abundance and morphology were similar (**Fig. 2A**), staining with both dyes was increased in PPBL B cells (**Fig. 2D**). Increased mitochondrial membrane potential was thus the sole difference captured in these experiments – suggestive of a subtle, yet robust (see **Fig. 1D**), difference in mitochondrial function that was driving the increased OCR of PPBL B cells.

Figure 2

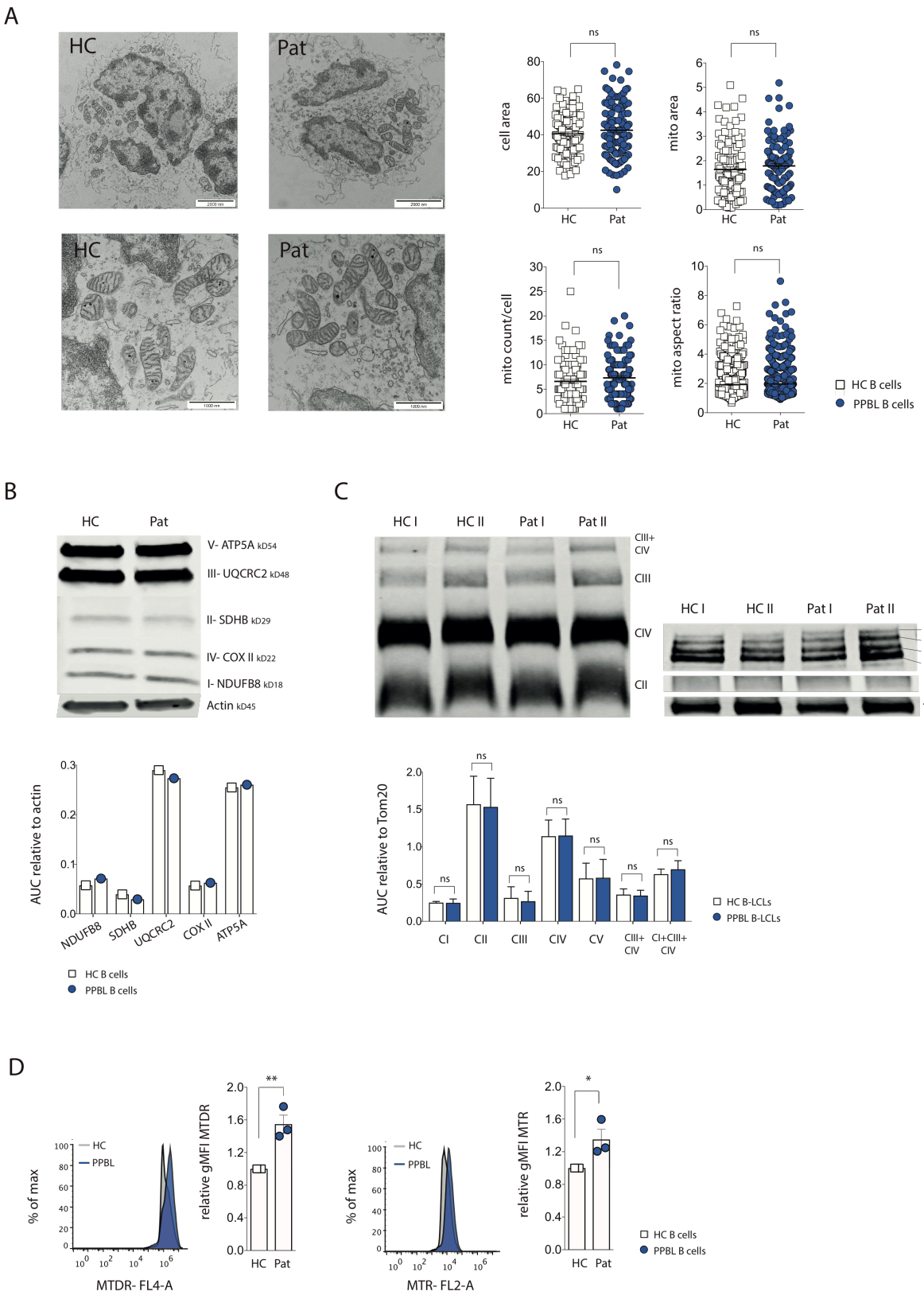
A
HC
Pat
HC
Pat
ns
cell area
mito area
mito count/cell
mito aspect ratio
HC
Pat
HC B cells
PPBL B cells
B
HC
Pat
V- ATP5A kD54
III- UQCRC2 kD48
II- SDHB kD29
IV- COX II kD22
I- NDUFB8 kD18
Actin kD45
AUC relative to actin
NDUFB8
SDHB
UQCRC2
COX II
ATP5A
HC B cells
PPBL B cells
C
HC I
HC II
Pat I
Pat II
CIII+ CIV
CIII
CIV
CII
I+III2
I+III2+ IV
CV
Tomm20
AUC relative to Tom20
CI
CII
CIII
CIV
CV
CIII+ CIV
CI+CIII+ CIV
HC B-LCLs
PPBL B-LCLs
D
HC
PPBL
% of max
MTDR- FL4-A
relative gMFI MTDR
MTR- FL2-A
relative gMFI MTR
HC B cells
PPBL B cells

Figure 2: Morphologic and biochemical characterization of mitochondria from PPBL patients.

(**A**) *Left panel:* Representative transmission electron microscopy images of a primary B cell from a HC and a PPBL patient. *Right panel:* Summary graphs of cell area; mitochondrial area; mitochondria count per cell, and mitochondrial aspect ratio from HCs (n = 3) and PPBL patients (n = 3). The aspect ratio of mitochondria was calculated as 'major axis' over 'minor axis'. Between 40 and 50 B cells were analyzed per individual.

(**B**) *Upper panel:* Immunoblot analysis (total cell lysates) of primary B cells from a HC and a PPBL patient. Blots were probed for Complex I (CI) subunit NDUFB8, Complex II (CII) subunit SDHB, Complex III (CIII) subunit Core 2, Complex IV (CIV) subunit I, Complex V (CV) ATP synthase subunit alpha, as well as actin. *Lower panel:* Quantification of the abundance of each complex subunit relative to actin.

(**C**) *Upper panel:* Representative blue native (BN)-PAGE immunoblot analysis of enriched mitochondria from B lymphoblastoid cell lines (B-LCLs) of HCs and PPBL patients, probed for CI (NDUFA9), CII (SDHA), CIII (UQCRC1), CIV (subunit I), CV (ATPB), and Tomm20. *Lower panel:* quantification of respiratory complexes and super-complexes (CI plus CIII plus CIV; CIII plus CIV) relative to Tomm20 in enriched mitochondria derived from B-LCLs from HCs (n = 3) and PPBL patients (n = 3). Individuals were tested in 4 independent experiments.

(**D**) Representative mitotracker deep red (MTDR) and mitotracker red (MTR) staining of primary B cells from a HC and a PPBL patient. The bar graph summarizes the geometric mean fluorescence intensity (gMFI) of MTDR and MTR of primary B cells from PPBL patients (n = 3) relative to HCs (n = 3).

Pooled data are represented as mean ± SEM. Statistical significance was assessed by Mann-Whitney test (**A**), unpaired t-test (**C**,**D**). *$p < 0.05$, **$p < 0.01$, ns, not significant.

Complex II is hyper-functional in PPBL B cells.

With no evidence for differential mitochondrial abundance, altered mitochondrial morphology, or differences in expression levels- or interaction of respiratory chain proteins, we next probed the function of each of the respiratory chain complexes individually. To that end, enzyme activity assays and metabolic flux studies were used, comparing the respective mitochondrial functions in healthy B cell lines and PPBL B cell lines. Testing enzyme activities individually, activities of complexes I, IV and V were identical in both cell populations. Activity of complex II was, however, robustly increased among the PPBL B cell lines (**Fig. 3A**), providing strong evidence for a specific mitochondria-intrinsic (i.e. complex II intrinsic) gain-of-function in these cells. To test the function of the respiratory complexes (I–IV) in their normal structural context, their contribution to the OCR was assessed in permeabilized cells [74]. Also in these metabolic flux-based studies, a selective increase in the function of complex II was observed (**Fig. 3B**). Inhibition of complex I with rotenone did not alter the difference of complex II-driven respiration between B cell lines from healthy donors and PPBL patients, establishing that increased oxygen consumption was indeed driven by complex II activity. Additional immunoblot analyses, assessing expression of Grim19, a subunit of complex I involved in electron transfer, as well SDHA, a major catalytic subunit of complex II, confirmed that protein abundance did not differ between patients and controls – further pointing to complex II hyper-function independent of protein quantity (**Fig. 3D**) [75,76]. Together these experiments established that an SDH/complex II gain-of-function phenotype was driving the increased OCR detected in the screening assays of the three patients with PPBL that were included in this study.

Figure 3

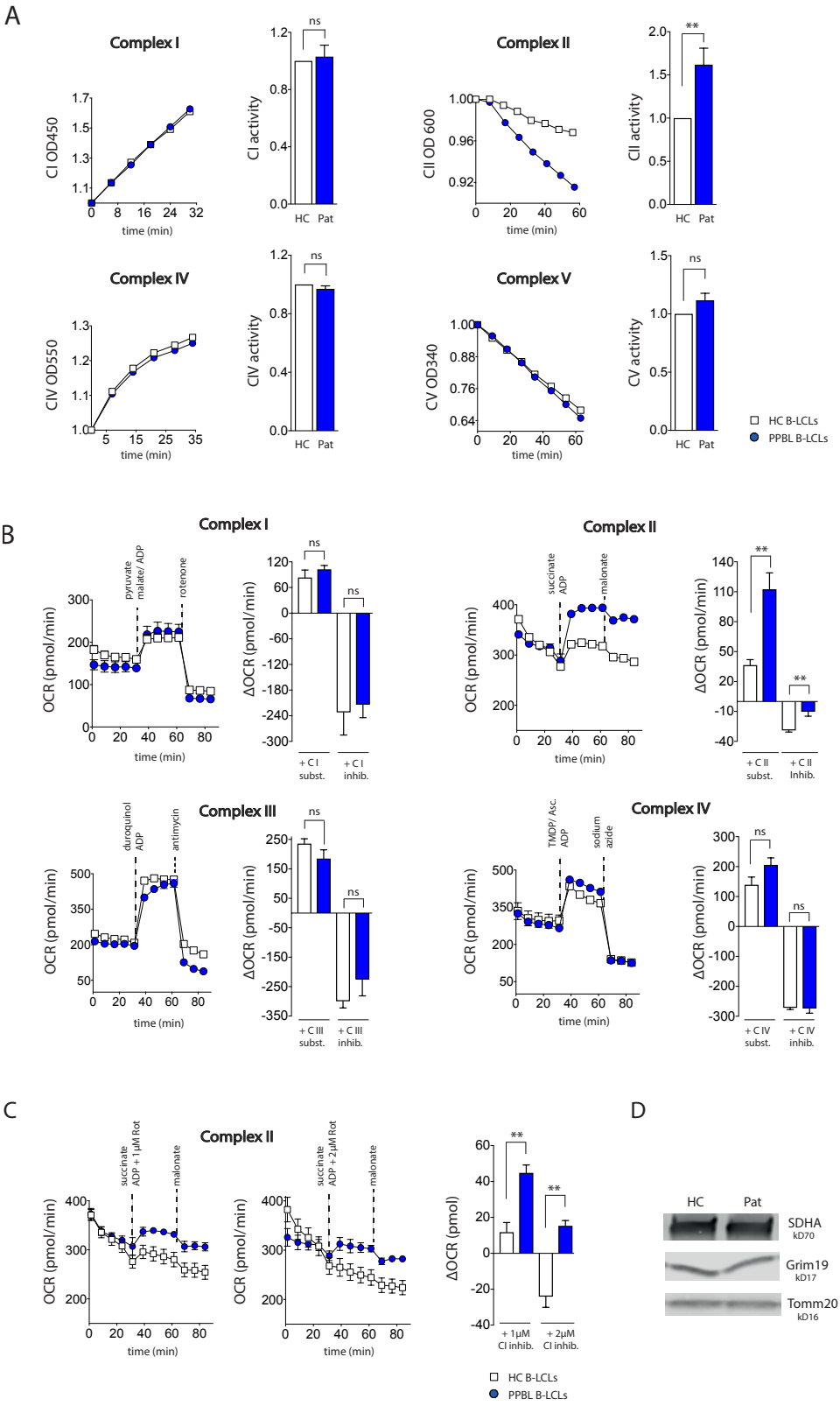
A
Complex I
CI OD450
time (min)
CI activity
HC Pat
ns
Complex II
CII OD 600
time (min)
CII activity
HC Pat
**
Complex IV
CIV OD550
time (min)
CIV activity
HC Pat
ns
Complex V
CV OD340
time (min)
CV activity
HC Pat
ns
HC B-LCLs
PPBL B-LCLs
B
Complex I
pyruvate malate/ ADP
rotenone
OCR (pmol/min)
time (min)
ΔOCR (pmol/min)
+ C I subst.
+ C I inhib.
Complex II
succinate ADP
malonate
OCR (pmol/min)
time (min)
ΔOCR (pmol/min)
+ C II subst.
+ C II Inhib.
Complex III
duroquinol ADP
antimycin
OCR (pmol/min)
time (min)
ΔOCR (pmol/min)
+ C III subst.
+ C III inhib.
Complex IV
TMDP/ Asc. ADP
sodium azide
OCR (pmol/min)
time (min)
ΔOCR (pmol/min)
+ C IV subst.
+ C IV inhib.
HC B-LCLs
PPBL B-LCLs
C
Complex II
succinate ADP + 1 µM Rot
malonate
OCR (pmol/min)
time (min)
succinate ADP + 2µM Rot
malonate
OCR (pmol/min)
time (min)
ΔOCR (pmol)
+ 1µM CI inhib.
+ 2µM CI inhib.
HC B-LCLs
PPBL B-LCLs
D
HC Pat
SDHA kD70
Grim19 kD17
Tomm20 kD16
AUC relative to Tom20
Grim19 SDHA
HC B-LCLs
PPBL B-LCLs

Figure 3: Activity of individual mitochondrial respiratory chain complexes in PPBL B cells.

(**A**) Representative activity-assays for CI, CII, CIV, and CV, depicted as changes of absorbance over time, comparing B-LCLs from HCs and PPBL patients. Summary graphs represent activity-rates of individual complexes from PPBL patients (n = 3) relative to those of HCs (n = 3-4).

(**B**) Representative OCRs of permeabilized B-LCLs from a HC and a PPBL patient following addition of complex specific substrates and inhibitors, as indicated (dashed lines). Summary graphs represent changes in OCR of permeabilized B-LCLs from HCs (n = 3-4) and PPBL patients (n = 3).

(**C**) Representative OCRs of permeabilized B-LCLs of a HC and a PPBL patient, following addition of succinate, ADP and rotenone or inhibitors, as indicated (dashed lines). The bar graph summarizes changes in OCR of permeabilized B-LCLs from HCs (n = 3) and PPBL patients (n = 3), following addition of CII substrate (succinate, ADP) and subsequent inhibition of CI with rotenone.

(**D**) Representative immunoblot analysis of isolated mitochondria from B-LCLs of a HC and one PPBL patient. Blots were probed for Complex I subunit GRIM19, Complex II subunit SDHA, and Tomm20. The bar graph summarizes the abundance of Grim19 and SDHA, normalized to Tomm20, in isolated mitochondria of B-LCLs derived from HCs (n = 4) and PPBL patients (n = 3).

Pooled data are represented as mean ± SEM. Statistical significance was assessed by unpaired t-test (**A-D**). *$p < 0.05$, ** $p < 0.01$, ns, not significant.

SDHA genetic alterations in PPBL study participants.

To gain insight into a possible genetic basis of the hyper-respiration phenotype observed in the PPBL study participants, whole exome sequencing (WES) of primary B cells was performed. The WES data were first interrogated for all known PID mutations. These analyses did not identify known plausible genetic abnormalities previously linked to a PID (data not shown). We then focused our investigations on rare genetic variants in genes encoding for mitochondrial proteins. This exploration revealed rare variants with a high CADD score in the SDHA gene of all three PPBL patients (**Tbl. 2**). The same mutations were also identified in DNA obtained by buccal swabs, suggesting germ-line origin. Since T cells (which also harbored the mutations – data not shown) did not show metabolic alterations, penetrance of the phenotype was established as being highly cell-type specific – as is true for most germ-line genetic diseases [77,78].

Table 2

Pat	Chr	Basepair	Ref	Alt	Zygosity	Gene symbol	Amino acid	rsID	ESP	CADD	Poly Phen2	SIFT score
1	5	225975	C	T	HET	SDHA	GG	rs61733344	0.001	20.4	NA	NA
8	5	223551	G	A	HET	SDHA	A45T	rs140736646	0	23	0.002	0.16
9	5	236513	C	T	HET	SDHA	A449V	rs201139275	NA	26.8	0.585	0.02

Pat = Patient; Chr = chromosome; Ref=reference sequence; Alt = alternative sequence; rsID = single nucleotide polymorphism database identifier; ESP = Grand Opportunity Exome Sequencing Project; CADD = Combined Annotation Dependent Depletion; PolyPhen = Polymorphism Phenotyping; SIFT = Sorting Intolerant from Tolerant.

SDHA (A45T) interacts more strongly with SDHB than wild type SDHA.

Based on this WES derived evidence for a genetic basis underlying gain-of-function in complex II, we aimed to investigate how such mutations might augment enzyme function at the level of the protein structure. In a proof of concept study we focused our efforts on modeling the functional impact of the A45T mutation (Patient #8). SDHA catalyzes oxidation of succinate to fumarate and transfers the resulting electrons to SDHB, which is followed by electron transport to the ubiquinone pool at SDHC-SDHD (succinate quinone reductase) [79]. The SDHA-SDHB complex retains succinate dehydrogenase activity also when dissociated from the membrane-anchoring subunits SDHC and SDHD [80]. We therefore focused our molecular dynamics (MD) simulations (A45T vs. wild type (wt)) on the interaction between SDHA and SDHB. Since the side-chain of Thr is highly hydrophilic, as opposed to Ala, we postulated that Thr at position 45 forms hydrogen bonds with SDHB, which may stabilize the complex and favor the electron transfer rate from flavin adenine dinucleotide (FAD) in SDHA to the iron-sulphur clusters in SDHB. H-bonds between the highly flexible SDHA N-terminal segment and SDHB formed randomly and, consequently, at the same rate in both wt and A45T mutated SDHA – with approximately 15-20 such events in each of ~600 trajectories that were analyzed (**Fig. 4A**, and supplementary Video **SV1**). However, whereas in the scenario with the wt sequence these interactions lasted 2-3 ns and involved mostly one atom pair, they lasted 10-12 ns and involved 2-3 atom-pairs in the case of the A45T mutation (**Fig. 4B**, and supplementary Video **SV1**). Together this resulted in a stronger hydrogen bond interaction between SDHA and SDHB in presence of the A45T mutation, reflected by an increase in the area under the curve of the hydrogen bonds between the two subdomains (**Fig. 4B**). Residues 1-4 of the N-terminus of SDHA form hydrogen bonds with the SDHB loop connecting β1 and β2. Not surprisingly, this loop in SDHB contains a highly conserved turn formed by Asp20-Pro21-Asp22. Indeed, the two residues Asp20 and Asp22 accounted for more than 90% of the interactions with the SDHA N-terminal segment (**Fig. S2A**). Such a prototypic interaction, in which Ala1, Ser2 and Lys4 of SDHA form hydrogen bonds or salt bridges with Asp20 and Asp22 of SDHB, is shown in **Figure 4C**. Mechanistically, Thr at the position 45 stabilized the SDHA-SDHB hydrogen bonds by higher interaction rates between Thr and residues on the adjacent surface of SDHA compared to wt. These interactions, involving Arg458, Phe459, Asp511, Arg512, and Met514, maintained the N-terminal segment in a position along the surface of SDHA, which favors the interactions with SDHB (**Fig. 4D**). Informed by these MD simulation data we aimed to further experimentally

assess the impact of the A45T mutation on combined SDHA *plus* SDHB activity (= SDH activity), *in vitro*. First, expression of mutant mRNA was confirmed in the cell line derived from the patient harboring this mutation (**Fig. 4E**, left panel). Next we measured combined SDHA *plus* SDHB activity spectrophotometrically in B cell lines form Patient #8 and from healthy controls. Indeed, in line with the MD simulation model, SDH activity was higher in B cell lines from the patient with the A45T mutation as compared to that in healthy control B cell lines (**Fig. 4E**, right panel). These data provided *in silico* structural evidence – aligning with *in vitro* experimental data – for a genetically imprinted molecular mechanism that drives excess function of SDH, namely by increasing interaction between the SDHA and SDHB, hence facilitating electron flux.

Figure 4

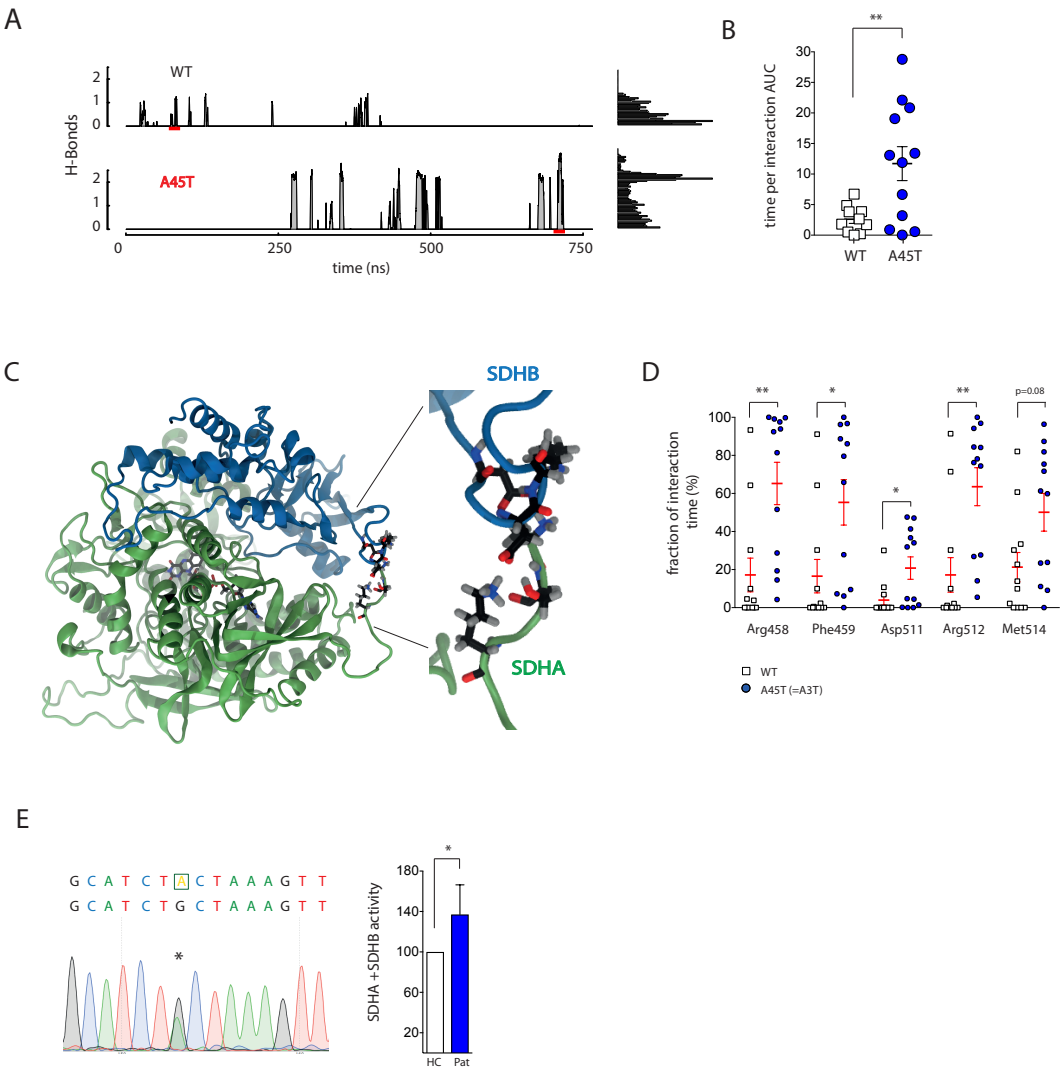
A
WT
A45T
H-Bonds
time (ns)
B
time per interaction AUC
WT
A45T
C
SDHB
SDHA
D
fraction of interaction time (%)
Arg458
Phe459
Asp511
Arg512
Met514
p=0.08
WT
A45T (=A3T)
E
G C A T C T A C T A A A G T T
G C A T C T G C T A A A G T T
SDHA +SDHB activity
HC
Pat

Figure 4: MD simulation of the interaction between SDHB and SDHA (wt vs. A45T).

(**A**) Number of hydrogen bonds formed over time between SDHB and residues 1-4 of SDHA, wild type (WT vs. A45T (= A3T in the functional protein product). Red segments highlight the trajectory extract shown in **Video V1** (https://www.dropbox.com/sh/cn69j7r0ropxx7t/AACgGjrcO1J9LT2UaS6lQTu1a?dl=0).Corresponding frequency distributions of the counted hydrogen bonds are shown in the insets.

(**B**) Time per interaction between SDHA and SDHB, calculated as area under the curve (AUC), of each individual simulation replica (WT vs. A45T).

(**C**) Molecular representation of the 'SDHA (green) SDHB (blue)' complex, shown in ribbons. The prosthetic group flavin adenine dinucleotide (FAD) is shown as sticks and CPK coloured (black arrowhead). A typical snapshot taken from the A45T trajectory is shown. Residues of the N-ter of SDHA within 2.5 Å of SDHB are shown as sticks and CPK coloured.

(**D**) Time fraction of simulated contacts between Threonine and adjacent SDHA residues (Arg458, Phe459, Asp511, Arg512 and Met514), as a percentage of the SDHA–SDHB interaction time in WT and A45T.

(**E**) *Left panel:* mRNA from B cells of Patient #8, carrying the A45T mutation. Asterisk indicated changes of nucleotide G to A at position 133. *Right panel:* Compound SDHA plus SDHB activity (enzyme complex derived from B-LCLs) from Patient #8 relative to HCs (n = 3). Compound SDHA–SDHB activity was independently tested 4 times in both, Patient #8 and each control subject.

Pooled data are represented as mean ± SEM. Statistical significance assessed by one-way ANOVA (**B**,**D**), Mann-Whitney test (**E**). *$p < 0.05$, ** $p < 0.01$, ns, not significant. See also **Figure S2**.

Fumarate accumulation in SDH hyper-functional PPBL B cells is fueled by glutaminolysis.

To gain insight into the metabolic landscape of B cells characterized by this newly identified 'complex II gain-of-function phenotype', we performed unbiased metabolomic analyses, comparing primary PPBL B cells with primary sorted marginal zone-like B cells from healthy individuals. The key finding of these experiments was a strong, and statistically highly significant accumulation of fumarate, i.e. the direct product of SDH. Malate, the first downstream metabolite of SDH in the TCA cycle (= product of fumarate hydratase), was also much more abundant (**Fig. 5A**, left panel) [81]. With the noticeable exception of succinate, all other TCA cycle metabolites captured in this assay were – albeit to a lesser extent than fumarate and malate – also more abundant in PPBL B cells than in healthy marginal zone-like B cells (**Fig. 5A**, left panel). This metabolite profile was in line with the increased functional activity of SDH identified in the previous experiments (**Figs. 3**,**4**). Since glutamate and α-KG were further significantly more abundant in PPBL B cells, the metabolomic data were suggesting increased glutaminolysis in PPBL B cells as compared to healthy marginal zone-like B cells (**Fig. 5A**, left and right panel). Several glycolytic intermediates were also more abundant in PPBL B cells (dihydroxyacetone phosphate, 2-phosphoglycerate, phosphoenolpyruvate and lactate). This was pointing to increased glycolysis in PPBL B cells – which was, however, not sufficiently pronounced to consistently drive increased ECAR values (**Fig. 1A**,**D**,**F**) and was also not associated with a more pronounced uptake of glucose (**Fig. 1G**). Of note, whereas the ratio of succinate over fumarate was increased in PPBL B cells, the ratio of α-KG to [fumarate & succinate] was not different between PPBL B cells and healthy marginal zone-like B cells since α-KG was also more abundant in these cells (**Fig. 5B**). To directly compare contribution of glucose- vs. glutamine-derived carbons to TCA cycle metabolites, metabolic tracing studies were performed on primary PPBL B cells, using uniformly labeled ^{13}C-glucose and ^{13}C-glutamine, respectively (**Fig. 5C**). These studies were informative in three ways. First, glutamine was found to significantly contribute to the fueling of the TCA cycle (abundant m+5 α-KG; m+4 succinate, m+4 fumarate, m+4 malate and m+4 citrate). Also at the glutamine-derived m+2 level (suggestive of more than one round of TCA cycling in the case of glutamine), glutamine and glucose similarly contributed to the pool of α-KG, succinate, fumarate and malate. Glutamine thus was an important TCA fuel source for PPBL B cells. Second, the presence of m+5 citrate pointed to reductive carboxylation of glutamine-derived α-KG as an anaplerotic source in PPBL B cells. Third, as also seen in the untargeted metabolomic analyses, we observed low m+2; m+4 succinate levels followed by

increased m+2; m+4 fumarate- and malate levels, both when considering glucose-derived or glutamine-derived carbons. Combined these metabolomic and tracing studies *(i)* identified glutamine as an important fuel source and an anaplerotic source of the TCA cycle in PPBL B cells, and *(ii)* confirmed accumulation of fumarate (and malate) – as a result of hyperactive SDH (**Figs. 3**,**4**).

Figure 5

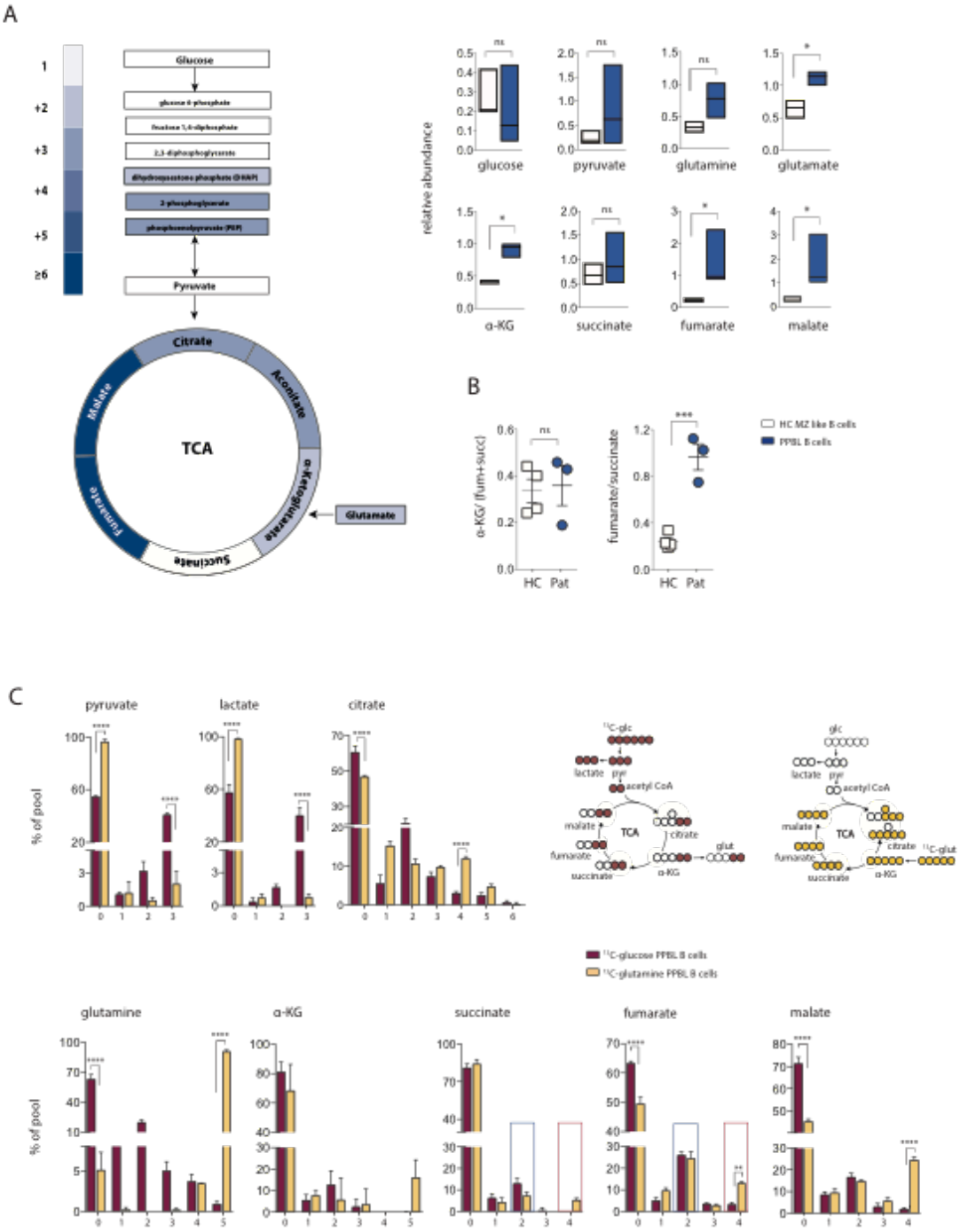
A
1
+2
+3
+4
+5
≥6
Glucose
Pyruvate
Citrate
Aconitate
α-Ketoglutarate
Succinate
Fumarate
Malate
TCA
Glutamate
relative abundance
glucose
pyruvate
glutamine
glutamate
α-KG
succinate
fumarate
malate
ns
*
B
α-KG/ (fum+succ)
fumarate/succinate
HC
Pat
***
HC MZ like B cells
PPBL B cells
C
pyruvate
lactate
citrate
% of pool
glutamine
α-KG
succinate
fumarate
malate
TCA
acetyl CoA
glut
¹³C-glucose PPBL B cells
¹³C-glutamine PPBL B cells

Figure 5: Metabolic characterization of PPBL B cells.

(**A**) *Left panel:* Significant fold change of glycolysis and the TCA cycle metabolites between primary B cells from PPBL patients (n = 3) and primary MZ-like B cells from HCs (4 samples pooled of n = 7 donors). *Right panels:* Relative abundance of glycolysis and TCA cycle metabolites in primary MZ-like B cells from HCs and primary B cells from PPBL patients (donors as in left panel).

(**B**) Ratio of abundance of α-ketoglutarate over (succinate + fumarate), and ratio of the abundance of fumarate over succinate, both in primary MZ-like B cells from HCs and primary B cells from PPBL patients (donors as in (A)).

(**C**) Metabolic tracing analysis of primary B cells from PPBL patients (n = 3) incubated for 6 hours with ^{13}C-glucose or ^{13}C-glutamine. Bar graphs show distribution of mass isotopomers, the scheme depicts the primary labelling of glucose- and glutamine-derived ^{13}C fuelling into the TCA cycle.

Pooled data are shown as mean ± SEM. Statistical significance was assessed by Welch's two sample t-test (**A**), unpaired t-test (**B**), and one-way ANOVA (**C**). *p < 0.05, ** p < 0.01, *** p < 0.001, **** p < 0.0001, ns, not significant.

PPBL B cells have an inflammatory transcriptional profile.

Having characterized the metabolic alteration and fuel usage of PPBL, we went on and investigated the transcriptional profile of primary PPBL B cells in comparison to their metabolically non-affected counterpart, i.e. marginal zone-like B cells from healthy blood donors. Of the 13'107 gene transcripts that were expressed, mRNA abundance of 1'878 genes (14.33%) differed in a statistically significant manner between the groups. Unsupervised hierarchical clustering of the samples revealed two groups corresponding to PPBL B cells and healthy marginal zone-like B cells (**Fig. 6A**). Establishing their close relationship, both groups were characterized by a gene profile typically found in marginal zone-like B cells (**Fig. 6B**) [82,83]. mRNA abundance of metabolic genes, i.e. those involved in glycolysis, glutamine metabolism and the TCA cycle, were similar in primary patient B cells and healthy marginal zone-like B cells (**Fig. 6C**, left panel, and **Fig. S3A**). Of note, also transcript levels of mitochondrial complex II genes were similar (**Fig. 6C,** right panel), as were those encoding for proteins in the other respiratory complexes (**Fig. S3B**).

In sharp contrast, gene products annotated to the inflammatory response, and the IL-6–Jak–Stat3 pathway, were enriched in the PPBL sample (**Fig. 6D**). Among the most differentially regulated inflammatory gene product was IL-6, a classic B cell cytokine, but also transcripts for TNF, IL-8, CCL5 and IL-1β were more abundantly expressed in PPBL B cells (**Fig. 6D**,**E**). These cytokines have been described as being produced by marginal zone-like B cells, reflecting the innate-like function of these cells as sensors of danger and regulators of the early immune response [84-86] [83,87-91]. From a clinical perspective, PPBL manifestations, particularly in Patient #9, pointed to the relevance of IL-6 (trigger of CRP production by hepatocytes) and IL-8 (key neutrophil chemoattractant) (specifically: chronic elevation – and intermittent spiking – of CRP levels; propensity for acute sterile inflammation mediated by neutrophils (polychondritis, small vessel vasculitis ('leukocytoclastic vasculitis')) (**Fig. 1B**, **Tbl. 1A**) [92-94]. Indeed, IL-6 and IL-8 were also increased at the protein level, both in the supernatant of non-activated as well as in activated B cell lines from PPBL patients, when compared to marginal zone-like B cell lines from healthy blood donors (**Fig. 6F**). Production of IL-8 by PPBL B cells was much more variable than that of IL-6, and less affected by stimulation with IL-21 and CD40L (**Fig. 6F**).

Figure 6

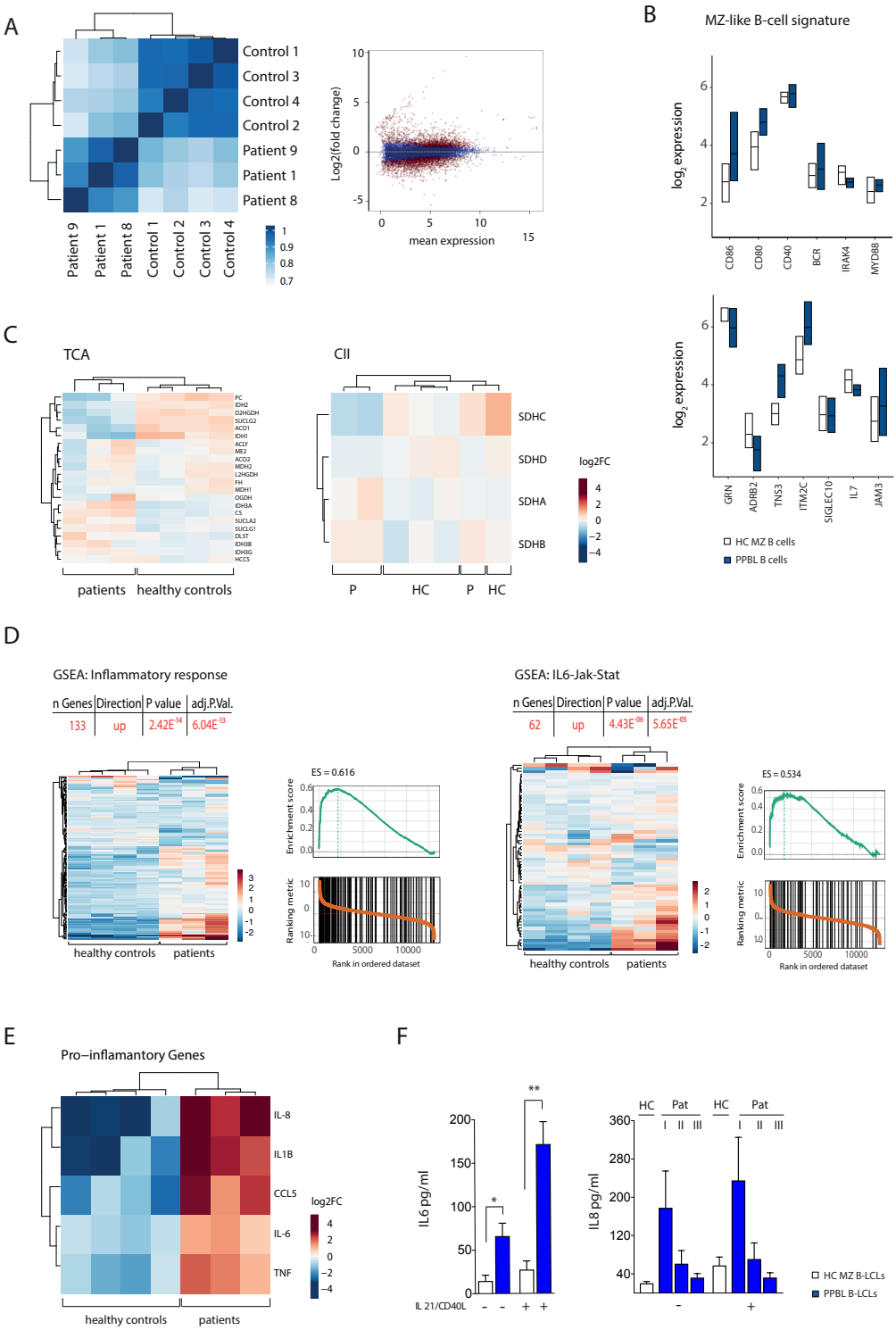
A
Control 1
Control 3
Control 4
Control 2
Patient 9
Patient 1
Patient 8
Patient 9
Patient 1
Patient 8
Control 1
Control 2
Control 3
Control 4
1
0.9
0.8
0.7
Log2(fold change)
mean expression
B
MZ-like B-cell signature
log2 expression
CD86
CD80
CD40
BCR
IRAK4
MYD88
GRN
ADRB2
TNS3
ITM2C
SIGLEC10
IL7
JAM3
HC MZ B cells
PPBL B cells
C
TCA
CII
patients
healthy controls
SDHC
SDHD
SDHA
SDHB
log2FC
P
HC
P
HC
D
GSEA: Inflammatory response
n Genes
Direction
P value
adj.P.Val.
133
up
2.42E-14
6.04E-13
ES = 0.616
Enrichment score
Ranking metric
Rank in ordered dataset
healthy controls
patients
GSEA: IL6-Jak-Stat
n Genes
Direction
P value
adj.P.Val.
62
up
4.43E-06
5.65E-05
ES = 0.534
Enrichment score
Ranking metric
Rank in ordered dataset
healthy controls
patients
E
Pro−inflamantory Genes
IL-8
IL1B
CCL5
IL-6
TNF
log2FC
healthy controls
patients
F
IL6 pg/ml
IL 21/CD40L
IL8 pg/ml
HC
Pat
HC
Pat
HC MZ B-LCLs
PPBL B-LCLs

Figure 6: Transcriptional profile of PPBL B cells.

(**A**) Hierarchical clustering (heatmap) of sample correlation and MA plot of transcriptome data from primary MZ-like B cells from HCs (n = 4) and primary B cells form PPBL patients (n = 3).

(**B**) mRNA abundance of MZ-like B cell marker-genes in primary MZ-like B cells from HCs and primary B cells form PPBL patients (donors as in (A)).

(**C**) Heatmap of relative expression of genes involved in the TCA cycle- (*left panel*) and genes encoding complex II (*right panel*), in primary MZ-like B cells from HCs and primary B cells form PPBL patients (donors as in (A)).

(**D**) Gene set enrichment analysis (GSEA) of inflammatory-response genes (*left panel*) and IL-6-Jak-Stat3 pathway genes (*right panel*), transcribed in primary B cells from PPBL patients, compared to MZ-like B cells from HCs (donors as in (A)).

(**E**) Heatmap of pro-inflammatory cytokine genes in primary MZ-like B cells from HCs and primary B cells form PPBL patients (donors as in (A)).

(**F**) Production of IL-6 and IL-8 protein by MZ-like B-LCLs from HCs (n = 3) and B-LCLs from PPBL patients (n = 3). Cytokines were quantified in culture supernatants of non-activated cells, or cells activated with IL-21 plus CD40L for 48 hours. Experiments were performed 3-4 times.

Pooled data are shown as mean ± SEM. Statistical significance was assessed by unpaired t-test (**F**). *$p < 0.05$, ** $p < 0.01$. See also **Figure S3**.

Fumarate accumulation can drive an inflammatory PPBL B cell phenotype.

Given the inflammatory transcriptome, and cytokine output, of PPBL B cells, we aimed to assess whether hyperactive SDH and increased cytokine production were linked. First, we probed the effect of the SDH inhibitor 3-nitropropionic acid (3-NPA) on mitochondrial respiration and IL-6 production. Increased OCR of PPBL B cell lines was efficiently reduced by inhibiting SDH with 3-NPA, both in intact cells (**Fig. 7A**), and in isolated mitochondria, i.e. in permeabilized cells provided with succinate and ADP (**Fig. 7B**). Importantly, both basal secretion as well as IL-21 plus CD40L driven production of IL-6, was diminished in PPBL B cell lines in the presence of 3-NPA (**Fig. 7C**). A genetic SDHA knockdown system was then utilized to specifically define the impact of SDH activity (more precisely the impact of the flavoprotein subunit of SDH that is responsible for transferring electrons from succinate to coenzyme Q (succinate + a quinone = fumarate + a quinol)) on production of IL-6. SDHA-targeting siRNA reduced SDHA protein expression-levels by approximately 40% (**Fig. 7D**), which was sufficient to reduce OCR of PPBL B cell lines by around 50% (**Fig. 7E**). Reduced SDHA activity was consistently linked with diminished IL-6 production in PPBL B cell lines from all three patients (**Fig. 7F**). These experiments established that SDHA in PPBL B cells was associated with their increased output of IL-6. The data, however, did not clarify whether an SDHA intrinsic feature, or the product of SDH *per se*, i.e. fumarate, were linked to the inflammatory output of PPBL B cells. To address this issue we genetically reduced expression of fumarate hydratase, the enzyme downstream of SDH converting fumarate to malate, in marginal zone-like B cell lines from healthy blood donors. Knockdown efficiency in these experiments was around 25% (**Fig. 7G**), which was sufficient to measurably increase fumarate abundance in these cells (**Fig. 7H**). In cell lines with high baseline production of IL-6, genetically engineering endogenous fumarate accumulation was indeed sufficient to enforce increased spontaneous production of IL-6 (**Fig. 7I**). These experiments thus identified fumarate accumulation as an inflammatory trigger in healthy marginal zone-like B cells with high baseline IL-6 production. At the same time, accumulation of malate – which was also observed in PPBL B cells with hyperactive SDH – was ruled out to be necessary for the inflammatory activity observed in PPBL B cells.

Fumarate drives succination of KEAP1 and Nrf-2 dependent transcription of IL-6.

Next we aimed to mechanistically link fumarate accumulation and inflammatory reprogramming of marginal zone-like B cells. Both succinate and fumarate have been assigned important roles in

balancing the activity of α-KG in its function as activator of histone and DNA demethylases. [49,50]. Increased expression of genes involved in histone demethylation has been linked with augmented cytokine production in monocytes cultured with fumarate [51]. To test whether in PPBL B cells a similar transcriptional response was induced by fumarate, we related the PPBL transcriptomes with the publically available fumarate-driven transcriptome of monocytes [51]. Gene expression profiles did, however, not correlate between these cell types (**Fig. 7J**). To screen for gross alterations of histone methylation, pan-H3 methylation was assessed between healthy primary B cells and primary PPBL B cells. In line with our finding that the ratio between α-KG and [succinate & fumarate] was not altered between these two cell types (**Fig. 5B**), no difference in pan-H3 methylation was detected (**Fig. 7K**). Irrespective of abundance of other TCA metabolites, succination of proteins by fumarate has been shown to alter protein function in macrophages and T cells, as well as non-immune cells [58,59,95]. Using an antibody recognizing the stable adduct formed by succination, i.e. S-2-(succino)cysteine (2SC), we went on and compared the protein succination profile of healthy primary B cells and primary PPBL B cells. Indeed, succination was more pronounced in PPBL B cells, with the most prominent band appearing at the size of 64 kD (**Fig. 7L**). In cancer cells with loss-of-function mutations in fumarate hydratase, and consecutive accumulation of fumarate, succination of Kelch-like ECH Associated Protein 1 (KEAP1) has been described [55,96]. Notably, KEAP1 has an apparent molecular mass of 60-64 kD in SDS-PAGE run under reducing conditions. A direct consequence of KEAP1 succination is stabilization of the transcription factor nuclear factor Nrf-2, with consecutive transcription of Nrf-2 regulated genes. Given the paucity of primary patient material we were so far unable to directly define the nature of this 64 kD protein by e.g. mass spectrometry. However, when stripping blots and re-staining with a monoclonal antibody against KEAP1, a band at the very same position was consistently revealed, highly suggestive of KEAP1 being succinated in PPBL B cells (**Fig. 7L**). To directly probe whether Nrf-2, released by succinated KEAP1, did regulate the production of the inflammatory cytokines IL-6 and IL-8 in PPBL B cells, the small molecule inhibitor, ML-385, was utilized. ML-385 is a recently developed, highly specific Nrf-2 inhibitor that is being investigated for use in patients suffering from cancers with loss-of-function mutations in KEAP1, or gain-of-function mutations in Nrf-2 [97-99]. Effectively, both in non-activated and – even more pronounced so – in activated PPBL B cells, ML-385 led to reduced production of both IL-6 and IL-8 (**Fig. 7M**). These data indicated that the inflammatory output of PPBL B cells was controlled in an Nrf-2 dependent manner.

In all, a molecular framework thus emerged with hyperactive SDH driving accumulation of fumarate, which in turn led to succination of KEAP1 and subsequent Nrf-2 driven inflammatory reprogramming of marginal zone-like B cells.

Figure 7

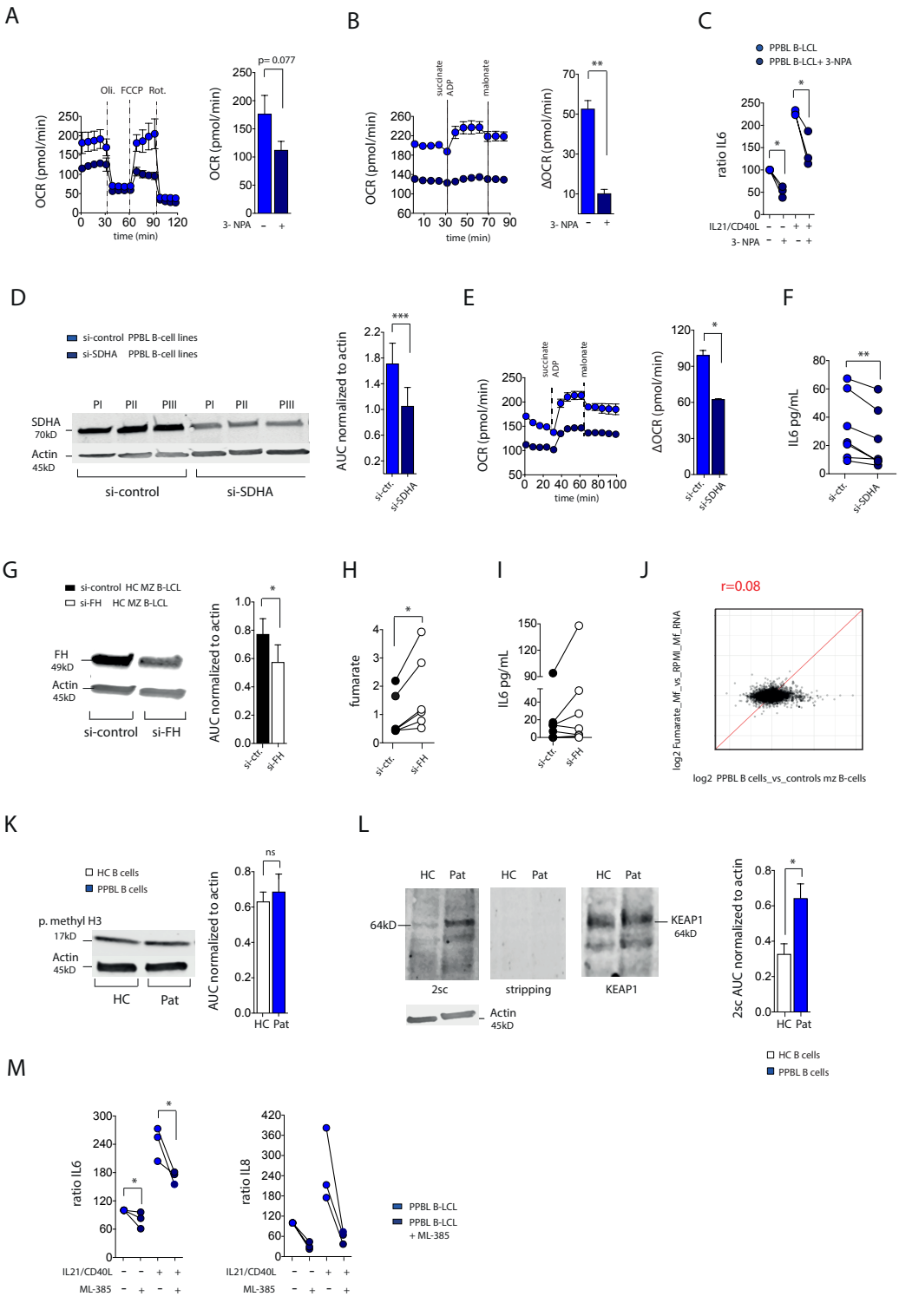
A
Oli. FCCP Rot.
OCR (pmol/min)
time (min)
p= 0.077
3- NPA
B
succinate
ADP
malonate
ΔOCR (pmol/min)
C
PPBL B-LCL
PPBL B-LCL+ 3-NPA
ratio IL6
IL21/CD40L
D
si-control PPBL B-cell lines
si-SDHA PPBL B-cell lines
PI PII PIII PI PII PIII
SDHA 70kD
Actin 45kD
si-control
si-SDHA
AUC normalized to actin
E
F
IL6 pg/mL
G
si-control HC MZ B-LCL
si-FH HC MZ B-LCL
FH 49kD
H
fumarate
I
J
r=0.08
log2 Fumarate_Mf_vs_RPMI_Mf_RNA
log2 PPBL B cells_vs_controls mz B-cells
K
HC B cells
PPBL B cells
p. methyl H3 17kD
ns
L
HC Pat
64kD
2sc
stripping
KEAP1
Actin 45kD
2sc AUC normalized to actin
M
ratio IL8
PPBL B-LCL
PPBL B-LCL + ML-385
ML-385

Figure 7: SDHA activity and inflammatory cytokine production.

(**A**) Representative mitochondrial perturbation profile of B-LCLs from a PPBL patient incubated with the SDHA inhibitor 3-nitropropionic acid (3-NPA), or left untreated, for 12 hours prior to the experiment. The bar graph summarizes basal mitochondrial respiration of B-LCLs from PPBL patients (n = 3) either exposed, or not exposed, to 3-NPA.

(**B**) Representative mitochondrial respiration profile of permeabilized B-LCLs from a PPBL patient prior to and following addition of complex II specific substrates (succinate, ADP) and the SDHA inhibitor, malonate, as indicated (dashed lines). B-LCLs were either exposed, or not exposed, to 3-NPA for 12 hours prior to the assay. The bar graph summarizes changes in OCR of permeabilized B-LCLs from PPBL patients (n = 3), following addition of CII substrate (succinate, ADP) and subsequent inhibition either exposed, or not exposed, to 3-NPA.

(**C**) Production of IL-6 by B-LCLs from PPBL patients (n = 3), measured in the culture supernatant of non-activated cells, or cells activated with IL-21 plus CD40L, in the presence or absence of 3-NPA for 48 hours. IL-6 ratios were calculated relative to baseline (untreated cells). IL-6 production from each PPBL patients was tested 2-3 times.

(**D**) Immunoblot analysis of total cell lysates from B-LCLs of PPBL patients (n = 3) transfected with control si-RNA, or SDHA si-RNA, and probed for SDHA protein abundance. The bar graph summarizes knockdown efficiency from (n = 6) independent experiments.

(**E**) Representative mitochondrial respiration profile of permeabilized B-LCLs from a PPBL patient prior to and following addition of complex II specific substrates and the SDHA inhibitor, malonate, as indicated (dashed lines). B-LCLs were treated with either control si-RNA or SDHA si-RNA prior to the assay. The bar graph summarizes changes in OCR of permeabilized control si-RNA or SDHA si-RNA treated B-LCLs from PPBL patients (n = 3).

(**F**) Production of IL-6 by B-LCLs from PPBL patients (n = 3) was quantified in cell culture supernatants of cells that were either treated with control si-RNA or SDHA si-RNA for 48 hours. Each patient cell line was tested 2 times.

(**G**) Representative immunoblot probing for fumarate hydratase in total cell lysate from MZ-like B-LCLs of a HC transfected either with control si-RNA or FH si-RNA. The bar graph summarizes knockdown efficiency from (n = 6) independent experiments.

(**H**) Production of IL-6 by MZ like B-LCLs from HCs (n = 3) was quantified in cell culture supernatants of cells transfected with either control si-RNA or FH si-RNA for 48 hours.

(**I**) Fumarate abundance in MZ like B-LCLs from HCs (n = 3) transfected with either control si-RNA or FH si-RNA for 48 hours. Each cell line was tested 2-3 times.

(**J**) Comparison of genes that were differentially expressed between non-treated and fumarate-treated monocytes (y-axis) and those differentially expressed between primary MZ-like B cells from HCs (n = 4) and primary B cells from PPBL patients (n=3) (x-axis) [51].

(**K**) Representative immunoblot probing for histone H3 methylation among primary B cells of a HC vs. primary B cells of a PPBL patient. The bar graph summarizes data from HCs (n=3) and PPBL patients (n = 3).

(**L**) Representative immunoblot analyses probing primary B cells of HC and PPBL patients for S-(2-succino)cysteine (2sc), followed by stripping and re-staining for KEAP1. The bar graph represents quantification of 2sc abundance at 64kD in primary B cells of HCs (n = 3) and PPBL patients (n = 3).

(**M**) Production of IL-6 and IL-8 by B-LCLs from PPBL patients (n = 3), measured in the culture supernatant of non-activated cells, or cells activated with IL-21 plus CD40L, in the presence or absence of the NRf-2 inhibitor, ML-385, for 48 hours. Each patient cell line was tested 2-3 times (exception: IL-8: only tested once for each patient cell line).

Pooled data are shown as mean ± SEM. Statistical significance was assessed by paired t-test (**A,B,D-I**), unpaired t-test (**K**,**L**) and Wilcoxon signed rank test (**C**,**M**). *$p < 0.05$, ** $p < 0.01$.

DISCUSSION

The potential of quantifying cellular metabolic pathway-activities as 'functional biomarkers' of cellular pathology has not been previously explored. Here, in a prospective screening approach, mitochondrial respiration was found to be higher in B cells from PAD patients. In the subset of patients with the most pronounced respiratory phenotype this observation guided the discovery of a new class of immune-pathologic deregulation, driven by fumarate accumulation. Specifically, hyper-respiration due to SDH gain-of-function was identified as the primary metabolic derangement causative of fumarate accumulation, protein succination and inflammatory reprogramming of marginal zone-like B cells in three independent patients with PPBL. Whether, and if so, *how* hyper-respiration in other PAD patients contributes to specific disease phenotypes remains to be defined. In principle, excess mitochondrial function may link with immunopathology in many ways, ranging from disrupted redox balance or inadequate ROS production to altered acetylation reactions; deregulation of epigenetic modifiers and – in light of the findings from this report – pathogenic succination events [35,55,96,100,101].

Notably, *gain*-of-function mutations in proteins of the respiratory chain have not been previously reported – making the here-described SDHA phenotype, and in particular the W45T mutation that we have characterized in detail, the first of its kind. Of note, in marginal zone-like B cells, chronic fumarate-driven production of IL-6 – a key B cell growth factor– may contribute, in addition to driving disease-typic B cell lymphocytosis, to the increased risk for B cell lymphoma noted in these patients [21,72,102-104]. If indeed overshoot SDH function were linked to tumorigenesis, this would assign this enzyme both tumor suppressing *and* tumor promoting properties, since SDH – alike several of the respiratory complex-encoding gene products – also has tumor *suppressor* properties [49,105-107]. Opportunities to therapeutically target overshoot mitochondrial function may emerge from this insight. In the case of patients with SDHA-driven fumarate accumulation as the metabolic cause for inflammatory reprogramming, repurposing drugs utilized in cancer patients might become an opportunity. Ionidamine, for example, is a well-tolerated compound that has been shown to inhibit succinate-ubiquinone reductase activity of complex II without fully blocking enzymatic activity [108,109]. In case of succination-dependent activation of the KEAP1–Nrf-2 axis, Nrf-2 inhibitors might prove successful [97-99]. However, since the KEAP1–Nrf-2 axis is driving cell-type specific transcriptional responses, mildly targeting the enzyme causative for fumarate accumulation might more precisely affect dysregulated transcriptional responses of marginal zone-like B cells [110].

Cell type specificity was indeed highlighted by a recent report that demonstrated, in LPS-stimulated macrophages, that itaconate – via alkylation of KEAP1 – drives an Nrf-2 dependent *anti*-inflammatory program in these cells. In contrast Nrf-2 mediated enhanced activity of the inflammasome has been reported in stimulated bone marrow derived macrophages [111]. Aligning with this finding several reports have shown that Nrf-2 deficiency alleviates pathogenesis of atherosclerosis, diabetes mellitus and obesity [112-114]. The importance of tight regulated Nrf-2 has been shown in a colitis model. Here overexpression of Nrf-2 in epithelial and myeloid cells exacerbates induced acute colitis, whereas chronic colitis was little affected by deregulated Nrf-2 [115].

Nrf-2 is a pleiotropic transcription factor, which not only regulates inflammation but also antioxidant response, proliferation and differentiation [116]. In several cancer types up regulated Nrf-2 expression has been linked with an uncontrolled proliferation and cancer progress [117-119]. Whether fumarate driven Nrf-2 activation is in involved in the pathogenesis of lymphoproliferation in PPBL cells has to be subject of further research.

The KEAP1–Nrf-2 system thus may emerge as a highly cell-type specific immunometabolic sensing system, integrating distinct metabolic activities with immunologic output.

It is intriguing to note that in multiple sclerosis and psoriasis, fumarate-esters are being used clinically for their *anti*-inflammatory properties [120-122]. In macrophages and T cells, pharmacologically increasing fumarate levels has recently been shown to drive succination events, including at the catalytic site of GAPDH [59]. Succination of GAPDH was found to curb aerobic glycolysis in these cells – thereby mediating anti-inflammatory activity [59]. By contrast, we now found that in PPBL B cells, endogenous accumulation of fumarate – via inadequate SDH activity – led to succination of KEAP1, which drove a *pro*-inflammatory transcriptional program. As glycolysis was not the major driver of the inflammatory output in these cells, PPBL B cells would thus be predicted to evade GAPDH-directed anti-inflammatory activity of fumarate-esters. In fact, exposure of PPBL patients to fumarate-esters might exacerbate inflammation.

This highlights the granularity of immunometabolic regulation and underscores the importance of understanding, in much detail, the distinct metabolic repertoires of immune cell subsets as we move towards clinical metabolic interventions.

In mice, marginal zone B cells are innate-like cells with the capacity to rapidly mount a first-line immune defensive response. As such these cells are poised to quickly produce a plethora of inflammatory cytokines. In humans, IgD^+ $CD27^+$ B cells are the assumed counterparts of rodent marginal zone B cells [83,123]. While the precise functional relevance of human marginal zone-like B cells remains unclear, they also rapidly produce inflammatory cytokines upon stimulation [82]. Aligning with the clinical phenotype of the PPBL patients in this study, mild fumarate accumulation in these inflammation-prone cells did drive non-regulated inflammatory cytokine output. Also when not intrinsically reprogrammed to produce inadequate amounts of inflammatory cytokines, marginal zone B cells have been shown to contribute to immunopathology. Specifically, IL-6 produced by marginal zone B cells has been demonstrated to exacerbate experimental systemic inflammatory responses [91]. It is further interesting that also in the context of autoimmunity, such as Sjogren's syndrome, marginal zone B cells have been proposed to contribute to disease [124,125].

Whether metabolic deregulation plays a role in the inadequate activation of marginal zone B cells in autoimmunity remains to be determined.

In each of the study participant with PPBL the genetic analysis identified a rare germline mutation in SDHA. All three individuals carried, however, different mutations. For the A45T mutation we provide a detailed structural model aligning with the experimentally observed gain-of-function (**Fig. 4**). *In silico*, the Thr at position 3 of the A45T-mutated SDHA contributed to only a small amount of inter-domain contacts, which did not support the hypothesis of a direct interaction between this residue and SDHB as the mechanism causing the enhanced interactions observed between the two proteins. One can speculate that a mechanism involves hydration of the N-terminus of SDHA. The higher hydrophilic nature of Thr, as compared to Ala, might increase, locally, the hydration level of the neighboring residues, thus stabilizing hydrophilic interactions between the SDHA N-terminal and the SDHB loop. This mechanism would be analogous to the driving force of protein folding nucleation [126]. The third mutation, rs61733344, was synonymous. The rs61733344 mutation was not in a splice site and it did not detectably affect protein expression (**Fig. 2C**, **3D**). Synonymous mutations were long believed to be functionally neutral. However, there is increasing evidence to the contrary. Indeed codon usage bias, i.e. unequal frequency at which synonymous codons are found, has been demonstrated in most genomes at above random levels [127]. Importantly, synonymous rare codons have also been

shown to play important functional roles in e.g. regulation of co-translational folding and covalent modifications, *in vivo* [128]. While much remains to be learned about the molecular events that connect synonymous codon usage, protein biogenesis and cell physiology, the here identified mutation might be subject to one such mechanism. The functional and clinical importance of synonymous mutations in human disease is underscored by the fact hat more than 50 human pathologies firmly associate with them, and that – overall – non-synonymous and synonymous mutations have a similar probability of associating with disease [129,130].

In summary, instructed by metabolic screening this study identified SDHA *gain*-of-function as a novel primary immune dysregulation, driving fumarate-dependent succination and inflammatory reprogramming of marginal zone-like B cells. Representing the first example of a *primary retrograde signaling pathology* (i.e. disruption of mitochondria-to-cellular-transcriptional regulation), our data point to therapeutic repurposing strategies by uncovering druggable targets – namely SDHA, Nrf-2 and IL-6 – along this dysregulated molecular axis.

MATERIALS AND METHODS

Study subjects

The study was approved by the *Ethikkommission Nordwest- und Zentralschweiz*; approval code EKNZ 2015-187. Fourteen patients, and 15 age and sex matched healthy controls, were prospectively recruited between July 2015 and December 2016. Inclusion criteria for patients were as follows: age >18 years; serum IgG level <7g/l, or IgG subclass deficiency (IgG_1 <4.9 g/l, IgG_2 <1.5 g/l, IgG_3 <0.2 g/l, IgG_4 <0.08 g/l). Patients evaluated by a Clinical Immunologist and classified as with a form of secondary antibody deficiency were excluded from the study.

Blood sample phenotyping and immunoglobulin quantification

After written informed consent, blood samples from patients and healthy controls (blood donor center, University Hospital Basel) were obtained. From all patients a differential white blood cell count, including total lymphocyte as well as T and B cell numbers, were obtained. B cells ($CD19^+$ in lymphocyte gate) were further phenotyped as follows: naïve B cells (IgD^+ $CD27^-$ IgM^+), marginal zone-like B cells (IgD^+ $CD27^+$ IgM^+), memory B cells (IgD^- $CD27^+$ IgM^-), transitional B cells (IgD^+ IgM^+ $CD38^+$), CD21 low B cells ($CD21^{low}$ $CD38^-$), and plasmablasts (IgD^- IgM^- $CD38^{++}$). T cells ($CD3^+$ in lymphocyte gate) were classified into: $CD4^+$ T cells, $CD8^+$ T cells, naïve ($CD27^+$ $CD45RO^-$) vs. central memory ($CD27^+$ $CD45RO^+$) vs. effector memory ($CD27^-$ $CD45RO^{+/-}$). Further, serum levels of total IgG and IgG subclasses (IgG_{1-4}); IgM; IgA, and IgE were quantified. All above experiments were performed at the GMP-certified central laboratory of the University Hospital Basel.

Cell sorting

To isolate immune cell subsets, peripheral blood mononuclear cells (PBMCs) were first isolated by standard density-gradient centrifugation (Lymphoprep Fresenus Kabi, Norway). B cells ($CD19^+$) and T cells ($CD3^+$) were then positively selected using magnetic beads (Miltenyi Biotec, Germany) according to manufacturer's instructions. For isolation of marginal zone-like B cells (MZ-like B cells), B cells ($CD19^+$) were stained with anti-CD27 brilliant Violet 605 (Biolegend, USA) and anti-IgD VioBlue (Miltenyi Biotec) mAb. $CD19^+CD27^+IgD^+$ B cells were sorted with a BD Influx cell sorter (BD Bioscience, USA). Prior to downstream experiments, cells were rested for 3

hours in RPMI-1640 medium (GIBCO, USA) containing 10% fetal bovine serum (FBS, GIBCO, USA), 50U/ml penicillin and 50 µg/ml streptomycin (GIBCO) (R10-FBS) at 37°C.

EBV transformed B lymphocyte cell lines

PBMCs or sorted MZ-like B cells were incubated with EBV-containing supernatant from B95-8 cells for 1 hour and additionally stimulated with CpG (1 µg/ml). Cyclosporine A (1 µg/ml) was added weekly for a total of four weeks to eliminate T cells. Purity of EBV transformed B cell lines, as defined by flow cytometry, was 92-98 % ($CD19^+$ and $CD3^-$).

Metabolic flux analysis

A Seahorse XF-96^e extracellular flux analyzer (Seahorse Bioscience, Agilent Technologies, USA) was used to define cellular oxygen consumption rates (OCR) and extracellular acidification rates (ECAR). Cells were plated ($3x10^5$ cells/well) onto plates coated with Cell-Tak (Corning, USA). Mitochondrial perturbation experiments were carried out by sequential addition of oligomycin (1 µM, Sigma-Aldrich, USA), FCCP (2 µM, Carbonyl cyanide 4-(trifluoromethoxy) phenylhydrazone, Sigma-Aldrich), and rotenone (1 µM, Sigma-Aldrich). OCR and ECAR were monitored in real time after injection of each compound. Basal respiration was calculated by subtracting non-mitochondrial respiration (rotenone rate) from baseline rate [47]. For measuring activation-induced glycolytic activity, primary B cells were activated with IL-21 (200 ng/ml, ImmunoTools, Germany) and CD40L (200 ng/ml, Sigma-Aldrich) injected into the flux analyzer via injection ports, and ECAR was monitored in real time. For monitoring OCR of intact mitochondria only, cells were resuspended in MAS buffer (70 mM sucrose, 220 mM mannitol, 10 mM KH_2PO_4, 5 mM $MgCl_2$, 2 mM HEPES, and 1 mM EGTA), then treated with the XF plasma membrane permeabilizer (Seahorse, Agilent Technologies), which was followed by addition of with pyruvate (5 mM) / malate (2.5 mM) / ADP (1 mM) and rotenone (1 µM) for monitoring CI-driven respiration; succinate (10 mM) / ADP (1 mM) with/without rotenone (1 µm / 2 µm) and malonate (0.04 mM) for monitoring CII-driven respiration; duroquinol (0.5 mM) / ADP (1 mM) and antimycin A (0.02 mM) for monitoring CIII-driven respiration; TMPD (0.5 mM) / Ascorbate 2 mM) / ADP (1 mM) and sodium azide (20 mM) (all from Sigma-Aldrich) for monitoring CIV-driven respiration. Changes in OCR upon substrate addition were calculated relative to the pre-injection rate. Changes in OCR upon inhibitor addition were calculated relative to the substrate rate.

2-NBDG uptake

To assess glucose-uptake, $5x10^5$ primary B cells were activated with IL-21 (200 ng/ml, ImmunoTools) and CD40L (200 ng/ml, Sigma-Aldrich) for 24 hours. Cells were then incubated in medium containing 20 μM 2-NBDG (Invitrogen) for 45 min and analyzed by flow cytometry.

Mitotracker red and mitotracker deep red

Primary B cells were incubated for 20 min at 37°C / 5% CO_2 with 100 nM Mitotracker red (MTR, Invitrogen), or 100 nM Mitotracker deep red (MTDR, Invitrogen), respectively. Cells were then washed twice in staining buffer (PBS plus 1% bovine serum albumin) and analyzed by flow cytometry.

Activity of individual respiratory chain complexes

To measure the activity of individual mitochondrial respiratory chain complexes, ELISA microplate assay kits (Abcam, UK) were used according to the manufacturer's instructions. In brief, CI activity was analyzed by tracking oxidation of NADH; CII by via the production of ubiquinone; CIV by tracing oxidation of cytochrome c; CV by assessing conversion of ATP to ADP and the coupled oxidation of NADH.

Electron microscopy

Transmission electron microscopy was performed at the Biozentrum (University of Basel). Primary B cells were sequentially fixed in 3% paraformaldehyde, 0.5% glutaraldehyde and 1% osmium tetraoxide, embedded and then cut into 60 nm sections. Micrographs (27'000x magnification) were obtained with a Morgagni 268 (FEI, Hillsboro OR, USA) transmission electron microscope operated at 80 kV. ImageJ software (NIH, Bethesda, USA) was used for measuring cell area; mitochondrial area, and mitochondrial length (major axis) and width (minor axis). The aspect ratio of mitochondria was calculated as 'major axis' over 'minor axis', an aspect ratio of 1 indicating a circular mitochondrial section.

Blue native PAGE

For isolation of mitoplasts, 8 x 10^6 B-LCLs were re-suspended in 100 µl of PBS, 32.5 µl of digitonin (8 mg/ml) was added and cells were incubated on ice for 10 min. Cold PBS (1 ml) was added and cells were centrifuged for 5 min at 10'000 x *g*. The pellet was resuspended in 100 µl of AA buffer (500 mM 6-aminohexanoic acid, 50 mM immidazole, 1 mM EDTA, pH 7) and 10 µl of a 10% digitonin solution was added. Next, cells were centrifuged for 30 min at 18'000 x *g*. Supernatant was harvested and 10 µl of sample buffer (5% blue G-250, 5% glycerol in AA Buffer) was added. Samples were stored at −80°C until use. BN-PAGE was performed as described [131]. Membranes were probed for anti-NDUFA9 mAb (20C11B11B11, Abcam), anti-complex II 70 kDA Fp mAb (459200, Invitrogen), Anti- UQCRC1 mAB (16D10AD9AH5) (110252, Abcam), anti-oxphos Complex IV Subunit I mAb (459600, Invitrogen), anti-ATPB antibody [3D5] - Mitochondrial Marker mAb (14730, Abcam) and Tom20 (FL-145) (sc11415, Santa Cruz Biotechnology, USA). For densitometry analysis, the ImageJ64 software was used. Band limits were determined using low-exposure images to efficiently distinguish individual bands.

Isolation of mitochondria

Cell pellets were washed with cold PBS and lysed using RIPA buffer (Thermo Fisher Scientific, Rockford IL, USA) containing protease and phosphatase inhibitors (Roche, Switzerland). To prepare mitochondrial fractions, 3x10^7 B-LCLs were collected and washed with buffer A (83 mM sucrose, 10 mM MOPS, pH 7.4). Cell pellets were then homogenized with 20 strokes in a tightly fitting glass-teflon homogenizer with 1 ml of buffer B (buffer A plus 10mM triethanolamine, 5% percoll, 0.01% digitonin, proteaseinhibitor, pH 7.4). Nuclei and unbroken cells were removed by centrifugation at 2'500 x *g* for 5 min. Supernatants were collected and centrifuged at 10'000 x *g* for 15 min. Mitochondria were then suspended in an appropriate volume of buffer C (300 mM sucrose, EGTA 1 mM, 20mM MOPS, proteaseinhibitor, pH 7.4) for storage at −80°C until use.

Immunoblot analysis

Protein concentrations were determined by BCA protein assay kit (Thermo Fisher Scientific). Whole-cell lysates or mitochondrial fractions were separated by 4-15% Mini Protean TGX Gel (Bio-Rad, Hercules CA, USA), and transferred to nitrocellulose using Trans-Blot Turbo Transfer

(Bio-Rad, Hercules CA, USA). Membranes were probed with anti-Grim19 mAb (ab110240), anit-NDFU8 mAb (ab110242), anti-SDHB mAb (ab14714), anti-Complex III subunit Core 2 mAb (ab14745), anti-Complex IV subunit II mAb (ab110258) and anti-ATPα mAb (ab14748) (all from Abcam), anti-SDHA mAb (119989), anti-FH mAb (4567), anti-KEAP1 mAb (8047), anti-NRF2 pAb (12721), pan-methyl-histone H3 (Lys9) mAb (4473) and anti-β-actin mAb (3700) (all from Cell Signaling, USA) and anti-2SC pAb (crb2005017e, Cambridge Research Biochemicals, UK). Blots were then stained with the appropriate secondary antibody (IRDye 800CW-conjugated goat polyclonal antibody against rabbit IgG (926-32211) or RDye 800CW-conjugated goat polyclonal antibody against mouse IgG (926-32219) from LI-COR). The Odyssey imaging system (LICOR) was used for detection, and the ImageJ software (1.48v) for quantification.

$^{13}C_6$ glucose and $^{13}C_6$ glutamine labeling

Primary B cells ($2x10^6$) from patients were plated onto 48 well plates in RPMI10-FBS with 4 mM U-^{13}C glucose or 4 mM U-^{13}C glutamine for 6 hours. Metabolites were extracted with 50 % MeOH / 30 % Acetonitrile. Isotopologue distribution was assessed by LC-MS. Metabolites were extracted from cells using ice-cold 80 % methanol, followed by sonication and removal of cellular debris by centrifugation at 4°C. Metabolite extracts were dried, derivatized as tert-butyldimethylsilyl (TBDMS) esters, and analyzed via GC-MS as previously described [132]. Uniformly deuterated myristic acid (750 ng / sample) was added as an internal standard following cellular metabolite extraction, and metabolite abundance was expressed relative to the internal standard, and normalized to cell number. Mass isotopomer distribution was determined using a custom algorithm developed at McGill University, Canada [133].

Metabolomics

Cell pellets from primary patient B cells and primary MZ-like B cells from healthy controls were isolated as described above, washed twice with cold PBS, snap frozen in EtOH containing dry ice and stored at −80°C. Metabolomic assays and analysis were performed by Metabolon Inc. (Durham, USA).

RNA sequencing

RNA from primary patient B cells and primary MZ-like B cells from healthy controls was isolated using nucleospin RNA kit (Macherey-Nagel, Germany) following manufacturer's instructions. RNA-seq was performed by Admera Health (USA). In brief, samples were isolated using ethanol precipitation. Quality check was performed using Tapestation RNA HS Assay (Agilent Technologies, USA) and quantified by Qubit RNA HS assay (Thermo Fisher Scientific). Ribosomal RNA depletion was performed with Ribo-zero Magnetic Gold Kit (MRZG12324, Illumina Inc., USA). Samples were randomly primed and fragmented based on manufacturer's recommendation (NEBNext® Ultra™ RNA Library Prep Kit for Illumina®). First strand was synthesized using Protoscript II Reverse Transcriptase with a longer extension period (40 minutes for 42˚C). All remaining steps for library construction were used according to the NEBNext® Ultra™ RNA Library Prep Kit for Illumina®. Illumina 8-nt dual-indices were used. Samples were pooled and sequencing on a HiSeq with a read length configuration of 150 paired-end.

Whole exome sequencing

The Oragene DNA OG-500 kit (DNA Genotek Inc., Canada) was used to collect saliva from patients, DNA was extracted using PrepIT L2P reagent (DNA Genotek Inc.). Whole exome sequencing (WES) was performed on B cells, T cells and saliva of all 3 PPBL patients included in this study. The input DNA concentration was 200 ng. DNA was quality controlled using Genomic DNA ScreenTape System (200 bp to 60000 bp) on a TapeStation 2200 (both Agilent Technologies). Sonication with a Covaris E220 was used to achieve fragmentation to 150-200bp. Sonication as well as library preparation was performed using the SureSelectXT Target Enrichment System for Illumina Paired-End Sequencing Library Protocol (Version C0, December 2016). SureSelectXT Reagent kits were used for library preparation (Agilent Technologies).
Exon-specific biotinylated oligonucleotides, SureSelect Human All Exon V6 (Agilent Technologies), were hybridized with the samples. Exons were pulled down using Dynabeads MyOne Streptavidin T1 magnetic beads (Thermo Fisher Scientific,). Paired-end 125 bp sequencing was performed on HiSeq 4000 Illumina platform. Output files from the sequencer were in FASTQ format. Paired-end sequencing resulted in two FASTQ files for each sample, forward and reverse. Forward and reverse FASTQ files were aligned to the reference genome (hg19) using Burrows-Wheeler Aligner (BWA_MEM). The output of BWA was a sequence

alignment map (SAM) file. Picard tools v2.7.1 (Picard_Tools_v2.7.1) was used to make a binary version of SAM files (=BAM files). Quality control was performed as per Genome Analysis Tool Kit (GATK) v3.5 guidelines from Broad Institute [134]. Each output BAM file was individually analyzed for variants from the reference genome using HaplotypeCaller from GATK resulting in a variant called file (VCF). Annotation of mutations was performed using Combined Annotation Dependent Depletion (CADD v1.3) and Variant effect predictor (VEP) programs [135,136]. Mutations of interest were visualized *in silico* using the Integrative Genomics Viewer (IGV) in order to confirm the mutation was in fact somatic and not present in controls [129,137]. The synonymous mutation was further investigated for splice altering, miRNA site, or mRNA structure altering, using NNSplice (NNSplice_v0.9), Human Splicing Finder (Human_Splice_Finder_v3.1), TargetScan (Target_Scan_v7.1) and Rescue ESE (RESCUE-ESE) [138,139]. Somatic analysis was performed using VarScan v2.3.9, Strelka Somatic Caller and MuTect2 [140,141] [142]. Annotation of somatic mutations from the 3 callers was performed using CADD v1.3 and VEP programs. Somatic mutations were visualized *in silico* using IGV.

End point PCR

Primers for the SDHA isoform as, forward 'GCA TTT GGC CTT TCT GAG GC' , reverse ' GCA CAG TCA GCC TCG TTC AA' ; and for the SDHA mutation as, forward ' CGA CTC CGG CGT GGT G' , reverse ' CTG CAA CAG TGT GTG ACC TG' were designed according the ncbi primer blast webtool (https://www.ncbi.nlm.nih.gov/tools/primer-blast/). PCR was run using Go Taq G2 DNA Polymerase (Promega, USA) with a GoTaq Green Master Mix (Promega) and the fragments were amplified in a thermal cycler (Professional Trio Thermocycler, Thermo Fisher Scientific). PCR products were separated in a 1.5% agarose gel and purified using Qiaquick Gel Extraction Kit (QIAGEN, Germany).

Construction of human SDHA and SDHB structures

Interaction between SDHA and SDHB were studied using MD simulations. To date no structures of human SDHA or SDHB have been published, yet the crystal structure of porcine heart mitochondrial complex II has been solved at 3.1 Å resolution (PDB code 4YTP) [143]. Porcine SDHA shares 94.58% protein identity with its human homolog (P31040), and the porcine and human SDHB proteins share high sequence homology as well. To generate a model of the human SDHA/SDHB complex, the sequence of the protein, as obtained from the US National Centre for

Biotechnology Information (https://www.ncbi.nlm.nih.gov - accessed 22nd February 2018), was submitted to the automated protein structure homology-modeling server, SWISS-MODEL [144]. Using the VMD and Chimera suites, a complex of human SDHA and SDHB was designed as follows: the N-ter SDHA segment was generated and grafted onto the SDHA structure as well the C-ter and both termini of SDHB [145] [146]. Using VMD, the 20 residues of the porcine SDHA/SDHB that differ from the human protein were changed into the corresponding human counterparts. Finally, two different models were generated, each extended at the N-ter with segments of sequence ASAKVSDSI (wt) and ASTKVSDSI (A3T = A45T mutation), respectively [145]. The A3T numbering refers to the functional protein, i.e. not including the transit peptide, which is removed during post-translational processing [147]. SDHA contains the prosthetic group flavin adenine dinucleotide (FAD), SDHB three iron-sulphur clusters. The structure of FAD was obtained from the Zinc library and their parameters were obtained through the CHARMM General Force Field (CGenFF) version 1.0.0 [148,149]. To study the SDHA/SDHB interaction, the FAD prosthetic group and the residues located in the cores of the subdomains were simulated with position restraints (with a force constant of 400 kJ mol^{-1} nm^{-2}). The proteins, including FAD, were virtually inserted in a water box, and K^+ and Cl^- ions added to simulate a physiological ionic concentration of 150 mM, and their respective number set to neutralize the system. Simulations were conducted with the GROMACS package, version 2016.3, using parallel tempering [150]. The CHARMM36 topology and parameter files were used to represent the protein and water was represented by the TIP3P model, whereas parameters for FAD were calculated with CGenFF [148,151]. The calculation of the electrostatic forces utilized the Particle-Mesh Ewald summation method, with a cutoff of 12 Å for the real space interactions, a 1.2 Å grid and 4^{th} order spline interpolation for the reciprocal space. The Lennard-Jones short and long-range cutoffs were set to 12 Å and 10 Å, respectively. Isotropic pressure at 1 bar was virtually maintained through coupling to a Parrinello-Rahman barostat, with a virtual compressibility of 4.5 x 10^{-5} bar and a coupling time of 5 ps [152]. Prior to the simulations, the systems were minimized with steepest descent. In order to further equilibrate the systems and allow water molecules to relax, a 25 ps simulation with a time step of 1 fs and with position restraints on the protein atoms was performed (with a force constant of 400 kJ mol^{-1} nm^{-2}). For parallel tempering, an ensemble of 48 temperatures in the range 310-385K was generated, whereas solute and solvent were weakly coupled to Nose-Hoover thermostats with coupling times of 1 ps [153,154]. Bonds with hydrogen atoms were constraint using the LINCS algorithm allowing usage of a time step of 2 fs. An

interval of 0.4 ns was set for the exchange probability calculation, thus providing enough time for SDHA-SDHB interactions to occur [155]. Each individual trajectory was ~22.5-23.0 ns long, totalizing 1100 and 1080 ns for the wt and the A3T mutant, respectively. The trajectories simulated for at a temperature lower than 360K were retained for the analyses, which were conducted either on the statistical platform R and specific R packages, GROMACS tools, or in-house Python scripts [156]. The readHBmap.py script was used to extract the hydrogen bond existences from the hydrogen bond Map files.

SDH activity

SDH activity (i.e. compound activity of SDHA and SDHB) was measured spectrophotometrically from the reduction of 2,6-diclorophenol-indophenol (DCPIP) by tracking the absorbance at 600 nm over 3 min. Frozen B-LCLs (5 x 10^6) were thawed and resuspended in 100 µl PBS on ice, protein concentration was determined, and the volume was adjusted to the sample with the lowest concentration. Each sample (20 µl) was suspended in 950 µl of buffer C1/C2 (25 mM potassium phosphate (K_2HPO_4) (pH = 7.2), 5 mM $MgCl_2$, 3 mM KCN, 2.5 mg/ml BSA) supplemented with 100 mM succinate and 0.1% Triton X-100, and incubated 10 min at room temperature. After addition of 6 µl 5 mM DCPIP, 2 µl 1 mg/ml of antimycin A and 2 µl 1 mM rotenone, samples were incubated for 2 min. Then, 6 µl of 10 mM phenazine methosulfate (PMS) was added and absorbance was measured. Compound activity of SDHA and SDHB was extrapolated using the following formula: [SDH activity = ((rate/min)/19.1) / sample volume x 1000 x dilution factor], where 19.1 is the molar extinction coefficient at 30°C (mM^{-1} cm^{-1}).

Cytokine measurements

B-LCLs (4 x 10^6) from patients, and MZ-like B-LCLs from healthy controls, were plated into 48 well plates. Cells were either left unstimulated (non-activated controls), or activated with IL-21 (40 ng/ml, ImmunoTools) and CD40L (40 ng/ml, Sigma-Aldrich). As indicated, 3-NPA (1.5 µm/ml, Sigma-Aldrich) or ML-385 (5 µm/ml, Sigma-Aldrich) was added. Supernatants were harvested 48 hours after activation, and concentrations of IL-6 and IL-8 were measured using Legendplex, human multiplex Panel (Biolegend), according to the manufacturer's instructions.

RNA mediated interference

B-LCLs ($2x10^6$) from patients, and MZ-like B-LCLs from healthy controls, were transfected with pools of siRNA targeting FH, SDHA, or control scrambled siRNA (QIAGEN) for 48 hours, using the AMAXA cell line V nucleofection kit (Lonza, Switzerland). Knockdown efficiency was assessed by immunoblot analysis.

Fumarate quantification

To measure cellular fumarate abundance, ELISA microplate assay kits (Abcam) were used according to manufacturer's instructions. In brief, $5x10^5$ MZ-like B-LCLs from healthy controls were homogenized in assay buffer and centrifuged at 13'000 x *g* for 10 min. Reaction mix was added to each standard and test sample, followed by an incubation of 1 hour at 37°C. Absorbance was measured at 450 nm using a microplate reader.

SUPPLEMENTAL MATERIAL

Figure S1

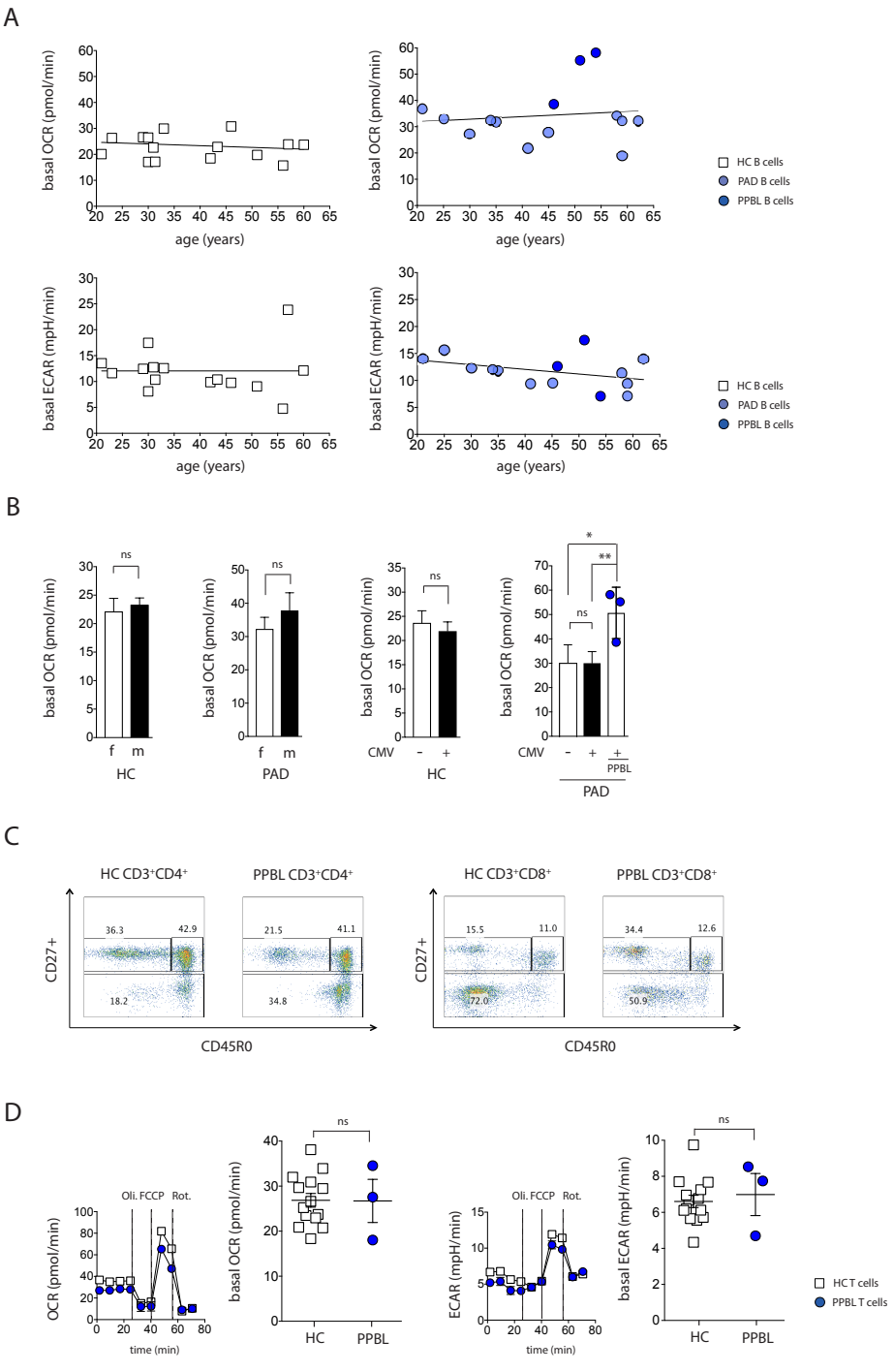
A
basal OCR (pmol/min)
age (years)
HC B cells
PAD B cells
PPBL B cells
basal ECAR (mpH/min)
B
ns
f m
HC
PAD
CMV - +
*
**
PPBL
C
HC CD3+CD4+
PPBL CD3+CD4+
HC CD3+CD8+
PPBL CD3+CD8+
CD27+
CD45R0
36.3
42.9
18.2
21.5
41.1
34.8
15.5
11.0
72.0
34.4
12.6
50.9
D
OCR (pmol/min)
Oli. FCCP Rot.
time (min)
basal OCR (pmol/min)
HC
PPBL
ECAR (mpH/min)
basal ECAR (mpH/min)
HC T cells
PPBL T cells

Figure S1:

(**A**) Age distribution of basal respiration (OCR) and basal glycolysis (ECAR) in primary B cells from HCs (n = 15) and PAD patients (n = 14).

(**B**) Basal respiration (OCR) in primary B cells from female vs. male and CMV^- vs. CMV^+ HCs (n = 12-15) and PAD patients (n = 13-14).

(**C**) Relative distribution of $CD4^+$ and $CD8^+$ T cells subsets from a HC and a PPBL patient.

(**D**) Representative mitochondrial perturbation profiles (OCR (left), ECAR (right)) of primary T cells from HCs and PPBL patients. Summary graphs present basal respiration (OCR – left) and basal glycolysis (ECAR – right) of primary T cells from HCs (n = 14) and PPBL patients (n = 3).

Pooled data are presented as mean ± SEM. Statistical significance was assessed by unpaired t-test (**B**,**D**). *$p < 0.05$, ** $p < 0.01$, ns, not significant.

Figure S2

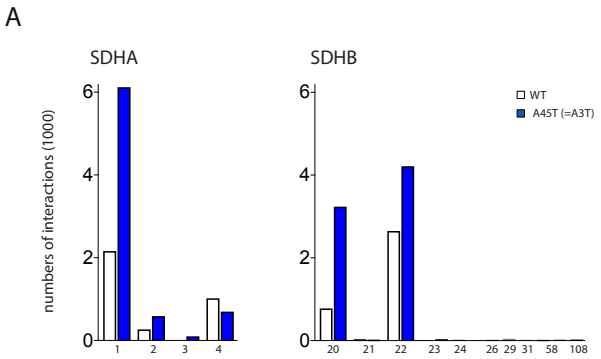

Figure S2:

(**A**) Frequency distributions of the residues from the N-terminal SDHA (left) and SDHB (right) involved in inter-domain hydrogen bonds in simulations with SDHA WT and SDHA A45T.

Figure S3

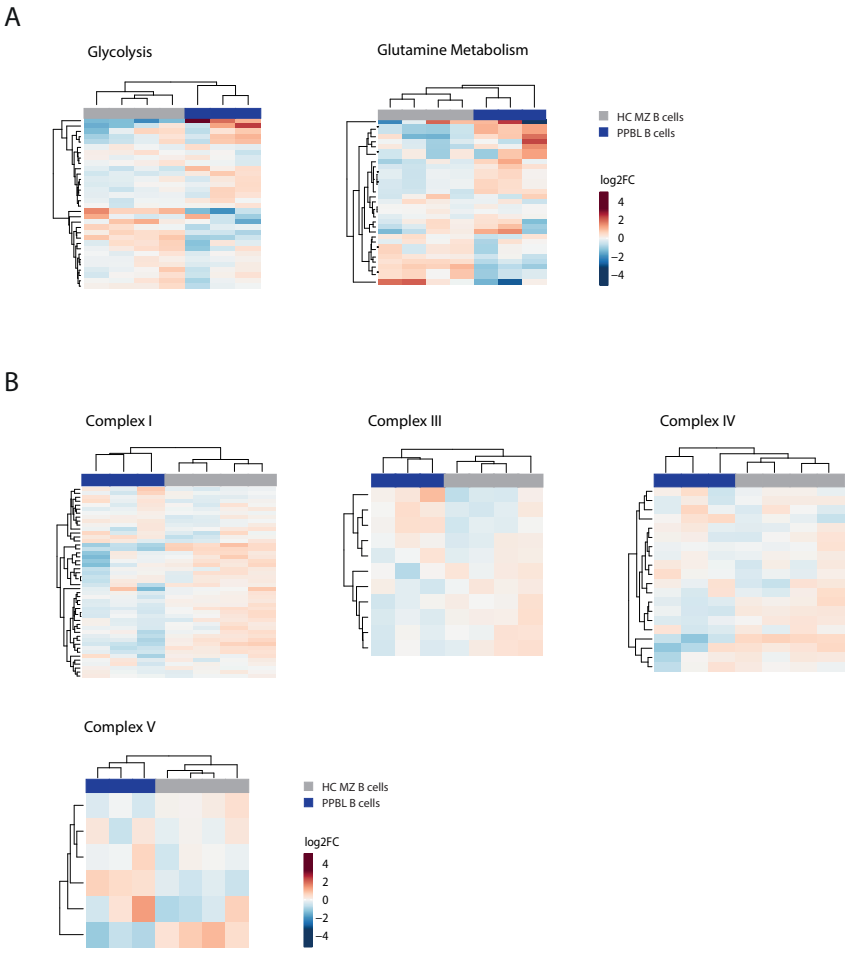

Figure S3:

(**A**) Heatmap-visualization; transcript abundance of genes involved in glycolysis and glutamine metabolism, in primary MZ-like B cells from HCs (n = 4) and primary B cells form PPBL patients (n = 3).

(**B**) Heatmap-visualization; transcript abundance of genes involved in respiratory complex I, III, IV and V in primary MZ-like B cells from HCs (n = 4) and primary B cells form PPBL patients (n = 3)

REFERENCES

1. Picard, C. *et al.* International Union of Immunological Societies: 2017 Primary Immunodeficiency Diseases Committee Report on Inborn Errors of Immunity. *Journal of Clinical Immunology* **38,** 96–128 (2018).
2. Fried, A. J. & Bonilla, F. A. Pathogenesis, diagnosis, and management of primary antibody deficiencies and infections. *Clin. Microbiol. Rev.* **22,** 396–414 (2009).
3. Durandy, A., Kracker, S. & Fischer, A. Primary antibody deficiencies. *Nat. Rev. Immunol.* **13,** 519–533 (2013).
4. Tsukada, S. *et al.* Deficient expression of a B cell cytoplasmic tyrosine kinase in human X-linked agammaglobulinemia. *Cell* **72,** 279–290 (1993).
5. Allen, R. C. *et al.* CD40 ligand gene defects responsible for X-linked hyper-IgM syndrome. *Science* **259,** 990–993 (1993).
6. Yel, L. *et al.* Mutations in the mu heavy-chain gene in patients with agammaglobulinemia. *N. Engl. J. Med.* **335,** 1486–1493 (1996).
7. Thompson, J. S. *et al.* BAFF-R, a newly identified TNF receptor that specifically interacts with BAFF. *Science* **293,** 2108–2111 (2001).
8. Grimbacher, B. *et al.* Homozygous loss of ICOS is associated with adult-onset common variable immunodeficiency. *Nat. Immunol.* **4,** 261–268 (2003).
9. van Zelm, M. C. *et al.* An antibody-deficiency syndrome due to mutations in the CD19 gene. *N. Engl. J. Med.* **354,** 1901–1912 (2006).
10. Conley, M. E. *et al.* Primary B cell immunodeficiencies: comparisons and contrasts. *Annu. Rev. Immunol.* **27,** 199–227 (2009).
11. Wood, P. *et al.* Recognition, clinical diagnosis and management of patients with primary antibody deficiencies: a systematic review. *Clin. Exp. Immunol.* **149,** 410–423 (2007).
12. Li, H., Ambade, A. & Re, F. Cutting edge: Necrosis activates the NLRP3 inflammasome. *J. Immunol.* **183,** 1528–1532 (2009).
13. Schiller, M. *et al.* Autoantigens are translocated into small apoptotic bodies during early stages of apoptosis. *Cell Death Differ.* **15,** 183–191 (2008).
14. Azizi, G. *et al.* Autoimmunity in Primary Antibody Deficiencies. *Int. Arch. Allergy Immunol.* **171,** 180–193 (2016).
15. Arason, G. J., Jorgensen, G. H. & Ludviksson, B. R. Primary immunodeficiency and autoimmunity: lessons from human diseases. *Scand. J. Immunol.* **71,** 317–328 (2010).
16. Chapel, H. *et al.* Common variable immunodeficiency disorders: division into distinct clinical phenotypes. *Blood* **112,** 277–286 (2008).
17. Cunningham-Rundles, C. & Bodian, C. Common variable immunodeficiency: clinical and immunological features of 248 patients. *Clin. Immunol.* **92,** 34–48 (1999).
18. de Miranda, N. F., Björkman, A. & Pan-Hammarström, Q. DNA repair: the link between primary immunodeficiency and cancer. *Ann. N. Y. Acad. Sci.* **1246,** 50–63 (2011).
19. Gangemi, S., Allegra, A. & Musolino, C. Lymphoproliferative disease and cancer among patients with common variable immunodeficiency. *Leuk. Res.* **39,** 389–396 (2015).
20. Friederichs, K., Schmitz, J., Weissenbach, M., Heinrich, P. C. & Schaper, F. Interleukin-6-induced proliferation of pre-B cells mediated by receptor complexes lacking the SHP2/SOCS3 recruitment sites revisited. *Eur. J. Biochem.* **268,** 6401–6407 (2001).
21. Jego, G. Interleukin-6 is a growth factor for nonmalignant human plasmablasts. *Blood* **97,** 1817–1822 (2001).
22. Levy, Y. *et al.* Interleukin 6 dependence of spontaneous in vitro differentiation of B cells from patients with IgM gammapathy. *Proc. Natl. Acad. Sci. U.S.A.* **87,** 3309–3313 (1990).

23. Chopra, G. S., Chitalkar, P. G. & Jaiprakash, M. P. Cytokines : as useful Prognostic Markers in Lymphoma Cases. *Med J Armed Forces India* **60,** 45–49 (2004).
24. Fischer, A. *et al.* Autoimmune and inflammatory manifestations occur frequently in patients with primary immunodeficiencies. *J. Allergy Clin. Immunol.* **140,** 1388–1393.e8 (2017).
25. Dimeloe, S., Burgener, A.-V., Grählert, J. & Hess, C. T-cell metabolism governing activation, proliferation and differentiation; a modular view. *Immunology* (2016). doi:10.1111/imm.12655
26. Hess, C. & Kemper, C. Complement-Mediated Regulation of Metabolism and Basic Cellular Processes. *Immunity* **45,** 240–254 (2016).
27. Bantug, G. R., Galluzzi, L., Kroemer, G. & Hess, C. The spectrum of T cell metabolism in health and disease. *Nat. Rev. Immunol.* **18,** 19–34 (2018).
28. Pearce, E. J. & Pearce, E. L. Immunometabolism in 2017: Driving immunity: all roads lead to metabolism. *Nat. Rev. Immunol.* **18,** 81–82 (2018).
29. Lunt, S. Y. & Vander Heiden, M. G. Aerobic glycolysis: meeting the metabolic requirements of cell proliferation. *Annu. Rev. Cell Dev. Biol.* **27,** 441–464 (2011).
30. Jellusova, J. *et al.* Gsk3 is a metabolic checkpoint regulator in B cells. *Nat. Immunol.* **18,** 303–312 (2017).
31. Boothby, M. & Rickert, R. C. Metabolic Regulation of the Immune Humoral Response. *Immunity* **46,** 743–755 (2017).
32. Carr, E. L. *et al.* Glutamine uptake and metabolism are coordinately regulated by ERK/MAPK during T lymphocyte activation. *J. Immunol.* **185,** 1037–1044 (2010).
33. Wang, R. *et al.* The transcription factor Myc controls metabolic reprogramming upon T lymphocyte activation. *Immunity* **35,** 871–882 (2011).
34. Jiang, S., Yan, W., Wang, S. E. & Baltimore, D. Let-7 Suppresses B Cell Activation through Restricting the Availability of Necessary Nutrients. *Cell Metab.* **27,** 393–403.e4 (2018).
35. Mehta, M. M., Weinberg, S. E. & Chandel, N. S. Mitochondrial control of immunity: beyond ATP. *Nat. Rev. Immunol.* **17,** 608–620 (2017).
36. Ernster, L. Mitochondria: a historical review. *The Journal of Cell Biology* **91,** 227s–255 (1981).
37. Martínez-Reyes, I. *et al.* TCA Cycle and Mitochondrial Membrane Potential Are Necessary for Diverse Biological Functions. *Mol. Cell* **61,** 199–209 (2016).
38. Bezawork-Geleta, A., Rohlena, J., Dong, L., Pacak, K. & Neuzil, J. Mitochondrial Complex II: At the Crossroads. *Trends Biochem. Sci.* **42,** 312–325 (2017).
39. Rutter, J., Winge, D. R. & Schiffman, J. D. Succinate dehydrogenase - Assembly, regulation and role in human disease. *Mitochondrion* **10,** 393–401 (2010).
40. Letts, J. A. & Sazanov, L. A. Clarifying the supercomplex: the higher-order organization of the mitochondrial electron transport chain. *Nat. Struct. Mol. Biol.* **24,** 800–808 (2017).
41. van der Windt, G. J. W. *et al.* Mitochondrial respiratory capacity is a critical regulator of CD8+ T cell memory development. *Immunity* **36,** 68–78 (2012).
42. Schurich, A. *et al.* Distinct Metabolic Requirements of Exhausted and Functional Virus-Specific CD8 T Cells in the Same Host. *Cell Rep* **16,** 1243–1252 (2016).
43. Tan, H. *et al.* Integrative Proteomics and Phosphoproteomics Profiling Reveals Dynamic Signaling Networks and Bioenergetics Pathways Underlying T Cell Activation. *Immunity* **46,** 488–503 (2017).
44. Tannahill, G. M. *et al.* Succinate is an inflammatory signal that induces IL-1β through HIF-1α. *Nature* **496,** 238–242 (2013).
45. Sena, L. A. *et al.* Mitochondria are required for antigen-specific T cell activation through

reactive oxygen species signaling. *Immunity* **38,** 225–236 (2013).
46. Ogura, M. *et al.* Mitochondrial reactive oxygen species suppress humoral immune response through reduction of CD19 expression in B cells in mice. *Eur. J. Immunol.* **47,** 406–418 (2017).
47. Gubser, P. M. *et al.* Rapid effector function of memory CD8+ T cells requires an immediate-early glycolytic switch. *Nat. Immunol.* **14,** 1064–1072 (2013).
48. Bantug, G. R. *et al.* Mitochondria-Endoplasmic Reticulum Contact Sites Function as Immunometabolic Hubs that Orchestrate the Rapid Recall Response of Memory CD8+T Cells. *Immunity* (2018). doi:10.1016/j.immuni.2018.02.012
49. Xiao, M. *et al.* Inhibition of α-KG-dependent histone and DNA demethylases by fumarate and succinate that are accumulated in mutations of FH and SDH tumor suppressors. *Genes Dev.* **26,** 1326–1338 (2012).
50. Laukka, T. *et al.* Fumarate and Succinate Regulate Expression of Hypoxia-inducible Genes via TET Enzymes. *J. Biol. Chem.* **291,** 4256–4265 (2016).
51. Arts, R. J. W. *et al.* Glutaminolysis and Fumarate Accumulation Integrate Immunometabolic and Epigenetic Programs in Trained Immunity. *Cell Metab.* **24,** 807–819 (2016).
52. Liu, P.-S. *et al.* α-ketoglutarate orchestrates macrophage activation through metabolic and epigenetic reprogramming. *Nat. Immunol.* **18,** 985–994 (2017).
53. Alderson, N. L. *et al.* S-(2-Succinyl)cysteine: a novel chemical modification of tissue proteins by a Krebs cycle intermediate. *Arch. Biochem. Biophys.* **450,** 1–8 (2006).
54. Ternette, N. *et al.* Inhibition of mitochondrial aconitase by succination in fumarate hydratase deficiency. *Cell Rep* **3,** 689–700 (2013).
55. Adam, J. *et al.* Renal cyst formation in Fh1-deficient mice is independent of the Hif/Phd pathway: roles for fumarate in KEAP1 succination and Nrf2 signaling. *Cancer Cell* **20,** 524–537 (2011).
56. Ooi, A. *et al.* An antioxidant response phenotype shared between hereditary and sporadic type 2 papillary renal cell carcinoma. *Cancer Cell* **20,** 511–523 (2011).
57. Castro-Vega, L. J., Lepoutre-Lussey, C., Gimenez-Roqueplo, A.-P. & Favier, J. Rethinking pheochromocytomas and paragangliomas from a genomic perspective. *Oncogene* **35,** 1080–1089 (2016).
58. Blatnik, M., Thorpe, S. R. & Baynes, J. W. Succination of proteins by fumarate: mechanism of inactivation of glyceraldehyde-3-phosphate dehydrogenase in diabetes. *Ann. N. Y. Acad. Sci.* **1126,** 272–275 (2008).
59. Kornberg, M. D. *et al.* Dimethyl fumarate targets GAPDH and aerobic glycolysis to modulate immunity. *Science* **17,** eaan4665 (2018).
60. Schon, E. A., DiMauro, S. & Hirano, M. Human mitochondrial DNA: roles of inherited and somatic mutations. *Nat. Rev. Genet.* **13,** 878–890 (2012).
61. Diaz, F., Kotarsky, H., Fellman, V. & Moraes, C. T. Mitochondrial disorders caused by mutations in respiratory chain assembly factors. *Semin Fetal Neonatal Med* **16,** 197–204 (2011).
62. Anderson, N. M., Mucka, P., Kern, J. G. & Feng, H. The emerging role and targetability of the TCA cycle in cancer metabolism. *Protein Cell* **9,** 216–237 (2018).
63. Marin, S. E. *et al.* Leigh syndrome associated with mitochondrial complex I deficiency due to novel mutations In NDUFV1 and NDUFS2. *Gene* **516,** 162–167 (2013).
64. Invernizzi, F. *et al.* A homozygous mutation in LYRM7/MZM1L associated with early onset encephalopathy, lactic acidosis, and severe reduction of mitochondrial complex III activity. *Hum. Mutat.* **34,** 1619–1622 (2013).

65. Mourier, A., Ruzzenente, B., Brandt, T., Kühlbrandt, W. & Larsson, N.-G. Loss of LRPPRC causes ATP synthase deficiency. *Human Molecular Genetics* **23,** 2580–2592 (2014).
66. Research, A. A. F. C. IDH Mutations Suppress T Cell-Mediated Antitumor Immunity. *Cancer Discov* **8,** OF17–OF17 (2018).
67. Chi, H. Regulation and function of mTOR signalling in T cell fate decisions. *Nat. Rev. Immunol.* **12,** 325–338 (2012).
68. Lucas, C. L. *et al.* Dominant-activating germline mutations in the gene encoding the PI(3)K catalytic subunit p110δ result in T cell senescence and human immunodeficiency. *Nat. Immunol.* **15,** 88–97 (2014).
69. Gordon, D. S., Jones, B. M., Browning, S. W., Spira, T. J. & Lawrence, D. N. Persistent polyclonal lymphocytosis of B lymphocytes. *N. Engl. J. Med.* **307,** 232–236 (1982).
70. Troussard, X. *et al.* Persistent polyclonal lymphocytosis with binucleated B lymphocytes: a genetic predisposition. *Br. J. Haematol.* **88,** 275–280 (1994).
71. Carr, R., Fishlock, K. & Matutes, E. Persistent polyclonal B-cell lymphocytosis in identical twins. *Br. J. Haematol.* **96,** 272–274 (1997).
72. Cornet, E. *et al.* Long-term follow-up of 111 patients with persistent polyclonal B-cell lymphocytosis with binucleated lymphocytes. *Leukemia* **23,** 419–422 (2009).
73. Bhagwandin, S. B., Weisenberg, E. S., Ozer, H. & Maker, A. V. Symptomatic Massive Splenomegaly in Persistent Polyclonal B-cell Lymphocytosis Requiring Splenectomy. *Open J Clin Med Case Rep* **1,** (2015).
74. Salabei, J. K., Gibb, A. A. & Hill, B. G. Comprehensive measurement of respiratory activity in permeabilized cells using extracellular flux analysis. *Nat Protoc* **9,** 421–438 (2014).
75. Huang, G. *et al.* GRIM-19, a cell death regulatory protein, is essential for assembly and function of mitochondrial complex I. *Mol. Cell. Biol.* **24,** 8447–8456 (2004).
76. Iverson, T. M., Maklashina, E. & Cecchini, G. Structural basis for malfunction in complex II. *J. Biol. Chem.* **287,** 35430–35438 (2012).
77. Barshir, R., Shwartz, O., Smoly, I. Y. & Yeger-Lotem, E. Comparative analysis of human tissue interactomes reveals factors leading to tissue-specific manifestation of hereditary diseases. *PLoS Comput Biol* **10,** e1003632 (2014).
78. Schaefer, M. H. & Serrano, L. Cell type-specific properties and environment shape tissue specificity of cancer genes. *Sci Rep* **6,** 20707 (2016).
79. Schwall, C. T., Greenwood, V. L. & Alder, N. N. The stability and activity of respiratory Complex II is cardiolipin-dependent. *Biochim. Biophys. Acta* **1817,** 1588–1596 (2012).
80. Hwang, M.-S., Rohlena, J., Dong, L.-F., Neuzil, J. & Grimm, S. Powerhouse down: Complex II dissociation in the respiratory chain. *Mitochondrion* **19 Pt A,** 20–28 (2014).
81. Teipel, J. W., Hass, G. M. & Hill, R. L. The substrate specificity of fumarase. *J. Biol. Chem.* **243,** 5684–5694 (1968).
82. Seifert, M. *et al.* Functional capacities of human IgM memory B cells in early inflammatory responses and secondary germinal center reactions. *Proc. Natl. Acad. Sci. U.S.A.* **112,** E546–55 (2015).
83. Cerutti, A., Cols, M. & Puga, I. Marginal zone B cells: virtues of innate-like antibody-producing lymphocytes. *Nat. Rev. Immunol.* **13,** 118–132 (2013).
84. Srivastava, M. D., Srivastava, R. & Srivastava, B. I. Constitutive production of interleukin-8 (IL-8) by normal and malignant human B-cells and other cell types. *Leuk. Res.* **17,** 1063–1069 (1993).
85. Sims-Mourtada, J. C. *et al.* In vivo expression of interleukin-8, and regulated on activation, normal, T-cell expressed, and secreted, by human germinal centre B lymphocytes. *Immunology* **110,** 296–303 (2003).

86. Dinarello, C. A. Immunological and inflammatory functions of the interleukin-1 family. *Annu. Rev. Immunol.* **27,** 519–550 (2009).
87. Jagannathan, M. *et al.* Toll-like receptors regulate B cell cytokine production in patients with diabetes. *Diabetologia* **53,** 1461–1471 (2010).
88. Sullivan, N. L. *et al.* Importance of the CCR5-CCL5 axis for mucosal Trypanosoma cruzi protection and B cell activation. *J. Immunol.* **187,** 1358–1368 (2011).
89. Liu, C.-C. *et al.* B cells facilitate platelet production mediated by cytokines in patients with essential thrombocythaemia. *Thromb. Haemost.* **112,** 537–550 (2014).
90. Tse, G. H. *et al.* Intrarenal B Cell Cytokines Promote Transplant Fibrosis and Tubular Atrophy. *Am. J. Transplant.* **15,** 3067–3080 (2015).
91. Honda, S.-I. *et al.* Marginal zone B cells exacerbate endotoxic shock via interleukin-6 secretion induced by Fcα/μR-coupled TLR4 signalling. *Nature Communications* **7,** 11498 (2016).
92. Zhang, D., Sun, M., Samols, D. & Kushner, I. STAT3 participates in transcriptional activation of the C-reactive protein gene by interleukin-6. *J. Biol. Chem.* **271,** 9503–9509 (1996).
93. Schenkel, E., Atkins, P. C., Yost, R. & Zweiman, B. Antigen-induced neutrophil chemotactic activity from sensitized lung. *J. Allergy Clin. Immunol.* **70,** 321–325 (1982).
94. Slaats, J., Oever, Ten, J., van de Veerdonk, F. L. & Netea, M. G. IL-1β/IL-6/CRP and IL-18/ferritin: Distinct Inflammatory Programs in Infections. *PLoS Pathog.* **12,** e1005973 (2016).
95. Ruecker, N. *et al.* Fumarase Deficiency Causes Protein and Metabolite Succination and Intoxicates Mycobacterium tuberculosis. *Cell Chem Biol* **24,** 306–315 (2017).
96. Kinch, L., Grishin, N. V. & Brugarolas, J. Succination of Keap1 and activation of Nrf2-dependent antioxidant pathways in FH-deficient papillary renal cell carcinoma type 2. *Cancer Cell* **20,** 418–420 (2011).
97. Bollong, M. J. *et al.* A Small Molecule Inhibits Deregulated NRF2 Transcriptional Activity in Cancer. *ACS Chem. Biol.* **10,** 2193–2198 (2015).
98. Singh, A. *et al.* Small Molecule Inhibitor of NRF2 Selectively Intervenes Therapeutic Resistance in KEAP1-Deficient NSCLC Tumors. *ACS Chem. Biol.* **11,** 3214–3225 (2016).
99. Zhu, J. *et al.* An overview of chemical inhibitors of the Nrf2-ARE signaling pathway and their potential applications in cancer therapy. *Free Radic. Biol. Med.* **99,** 544–556 (2016).
100. Wagner, G. R. & Payne, R. M. Mitochondrial Acetylation and Diseases of Aging. *Journal of Aging Research* **2011,** 1–13 (2011).
101. Alcalá, M. *et al.* Increased inflammation, oxidative stress and mitochondrial respiration in brown adipose tissue from obese mice. *Sci Rep* **7,** 2169 (2017).
102. Roy, J., Ryckman, C., Bernier, V., Whittom, R. & Delage, R. Large cell lymphoma complicating persistent polyclonal B cell lymphocytosis. *Leukemia* **12,** 1026–1030 (1998).
103. Tohyama, N. Growth autonomy and tumorigenicity of interleukin 6-dependent B cells transfected with interleukin 6 cDNA. *J. Exp. Med.* **171,** 389–400 (1990).
104. Mine, S. *et al.* Interleukin-6-dependent growth in a newly established plasmablastic lymphoma cell line and its therapeutic targets. *Sci Rep* **7,** 2323 (2017).
105. Burnichon, N. *et al.* SDHA is a tumor suppressor gene causing paraganglioma. *Human Molecular Genetics* **19,** 3011–3020 (2010).
106. Su, C.-Y., Chang, Y.-C., Yang, C.-J., Huang, M.-S. & Hsiao, M. The opposite prognostic effect of NDUFS1 and NDUFS8 in lung cancer reflects the oncojanus role of mitochondrial

complex I. *Sci Rep* **6,** 85 (2016).
107. Kim, H.-C., Chang, J., Lee, H. S. & Kwon, H. J. Mitochondrial UQCRB as a new molecular prognostic biomarker of human colorectal cancer. *Exp. Mol. Med.* **49,** e391 (2017).
108. Guo, L. *et al.* Inhibition of Mitochondrial Complex II by the Anticancer Agent Lonidamine. *J. Biol. Chem.* **291,** 42–57 (2016).
109. Nath, K. *et al.* Mechanism of antineoplastic activity of lonidamine. *Biochim. Biophys. Acta* **1866,** 151–162 (2016).
110. Mills, E. L. *et al.* Itaconate is an anti-inflammatory metabolite that activates Nrf2 via alkylation of KEAP1. *Nature* (2018). doi:10.1038/nature25986
111. Zhao, C., Gillette, D. D., Li, X., Zhang, Z. & Wen, H. Nuclear factor E2-related factor-2 (Nrf2) is required for NLRP3 and AIM2 inflammasome activation. *J. Biol. Chem.* **289,** 17020–17029 (2014).
112. Barajas, B. *et al.* NF-E2-related factor 2 promotes atherosclerosis by effects on plasma lipoproteins and cholesterol transport that overshadow antioxidant protection. *Arterioscler. Thromb. Vasc. Biol.* **31,** 58–66 (2011).
113. Chartoumpekis, D. V. *et al.* Nrf2 represses FGF21 during long-term high-fat diet-induced obesity in mice. *Diabetes* **60,** 2465–2473 (2011).
114. Pi, J. *et al.* Deficiency in the nuclear factor E2-related factor-2 transcription factor results in impaired adipogenesis and protects against diet-induced obesity. *J. Biol. Chem.* **285,** 9292–9300 (2010).
115. Gerstgrasser, A. *et al.* Cell-specific Activation of the Nrf2 Antioxidant Pathway Increases Mucosal Inflammation in Acute but Not in Chronic Colitis. *J Crohns Colitis* **11,** 485–499 (2017).
116. Murakami, S. & Motohashi, H. Roles of Nrf2 in cell proliferation and differentiation. *Free Radic. Biol. Med.* **88,** 168–178 (2015).
117. Fan, Z. *et al.* Nrf2-Keap1 pathway promotes cell proliferation and diminishes ferroptosis. *Oncogenesis* **6,** e371–e371 (2017).
118. Kerins, M. J. & Ooi, A. A catalogue of somatic NRF2 gain-of-function mutations in cancer. *Sci Rep* **8,** 12846 (2018).
119. Menegon, S., Columbano, A. & Giordano, S. The Dual Roles of NRF2 in Cancer. *Trends Mol Med* **22,** 578–593 (2016).
120. Kolbach, D. N. & Nieboer, C. Fumaric acid therapy in psoriasis: results and side effects of 2 years of treatment. *J. Am. Acad. Dermatol.* **27,** 769–771 (1992).
121. Altmeyer, P. J. *et al.* Antipsoriatic effect of fumaric acid derivatives. Results of a multicenter double-blind study in 100 patients. *J. Am. Acad. Dermatol.* **30,** 977–981 (1994).
122. Lundy, S. K. *et al.* Dimethyl fumarate treatment of relapsing-remitting multiple sclerosis influences B-cell subsets. *Neurol Neuroimmunol Neuroinflamm* **3,** e211 (2016).
123. Weller, S. *et al.* Human blood IgM 'memory' B cells are circulating splenic marginal zone B cells harboring a prediversified immunoglobulin repertoire. *Blood* **104,** 3647–3654 (2004).
124. Daridon, C. *et al.* Identification of transitional type II B cells in the salivary glands of patients with Sjögren's syndrome. *Arthritis Rheum.* **54,** 2280–2288 (2006).
125. Shen, L. *et al.* Central role for marginal zone B cells in an animal model of Sjogren's syndrome. *Clin. Immunol.* **168,** 30–36 (2016).
126. Jorgensen, W. L., Chandrasekhar, J., Madura, J. D., Impey, R. W. & Klein, M. L. Comparison of simple potential functions for simulating liquid water. *The Journal of Chemical Physics* **79,** 926–935 (1983).

127. Plotkin, J. B. & Kudla, G. Synonymous but not the same: the causes and consequences of codon bias. *Nat. Rev. Genet.* **12,** 32–42 (2011).
128. Chaney, J. L. & Clark, P. L. Roles for Synonymous Codon Usage in Protein Biogenesis. *Annu Rev Biophys* **44,** 143–166 (2015).
129. Thorvaldsdóttir, H., Robinson, J. T. & Mesirov, J. P. Integrative Genomics Viewer (IGV): high-performance genomics data visualization and exploration. *Brief. Bioinformatics* **14,** 178–192 (2013).
130. Hunt, R. C., Simhadri, V. L., Iandoli, M., Sauna, Z. E. & Kimchi-Sarfaty, C. Exposing synonymous mutations. *Trends Genet.* **30,** 308–321 (2014).
131. Wittig, I., Braun, H.-P. & Schägger, H. Blue native PAGE. *Nat Protoc* **1,** 418–428 (2006).
132. Faubert, B. *et al.* Loss of the tumor suppressor LKB1 promotes metabolic reprogramming of cancer cells via HIF-1α. *Proc. Natl. Acad. Sci. U.S.A.* **111,** 2554–2559 (2014).
133. McGuirk, S. *et al.* PGC-1α supports glutamine metabolism in breast cancer. *Cancer Metab* **1,** 22 (2013).
134. McKenna, A. *et al.* The Genome Analysis Toolkit: a MapReduce framework for analyzing next-generation DNA sequencing data. *Genome Research* **20,** 1297–1303 (2010).
135. Kircher, M. *et al.* A general framework for estimating the relative pathogenicity of human genetic variants. *Nat. Genet.* **46,** 310–315 (2014).
136. McLaren, W. *et al.* The Ensembl Variant Effect Predictor. *Genome Biol.* **17,** 122 (2016).
137. Robinson, J. T. *et al.* Integrative genomics viewer. *Nat. Biotechnol.* **29,** 24–26 (2011).
138. Reese, M. G., Eeckman, F. H., Kulp, D. & Haussler, D. Improved splice site detection in Genie. *J. Comput. Biol.* **4,** 311–323 (1997).
139. Agarwal, V., Bell, G. W., Nam, J.-W. & Bartel, D. P. Predicting effective microRNA target sites in mammalian mRNAs. *Elife* **4,** 101 (2015).
140. Koboldt, D. C. *et al.* VarScan 2: somatic mutation and copy number alteration discovery in cancer by exome sequencing. *Genome Research* **22,** 568–576 (2012).
141. Cibulskis, K. *et al.* Sensitive detection of somatic point mutations in impure and heterogeneous cancer samples. *Nat. Biotechnol.* **31,** 213–219 (2013).
142. Saunders, C. T. *et al.* Strelka: accurate somatic small-variant calling from sequenced tumor-normal sample pairs. *Bioinformatics* **28,** 1811–1817 (2012).
143. Inaoka, D. K. *et al.* Structural Insights into the Molecular Design of Flutolanil Derivatives Targeted for Fumarate Respiration of Parasite Mitochondria. *Int J Mol Sci* **16,** 15287–15308 (2015).
144. Biasini, M. *et al.* SWISS-MODEL: modelling protein tertiary and quaternary structure using evolutionary information. *Nucleic Acids Res.* **42,** W252–8 (2014).
145. Humphrey, W., Dalke, A. & Schulten, K. VMD: visual molecular dynamics. *J Mol Graph* **14,** 33–8– 27–8 (1996).
146. Pettersen, E. F. *et al.* UCSF Chimera--a visualization system for exploratory research and analysis. *J Comput Chem* **25,** 1605–1612 (2004).
147. Huo, X. *et al.* Preliminary molecular characterization and crystallization of mitochondrial respiratory complex II from porcine heart. *FEBS J.* **274,** 1524–1529 (2007).
148. Vanommeslaeghe, K. *et al.* CHARMM general force field: A force field for drug-like molecules compatible with the CHARMM all-atom additive biological force fields. *J Comput Chem* **31,** 671–690 (2010).
149. Irwin, J. J., Sterling, T., Mysinger, M. M., Bolstad, E. S. & Coleman, R. G. ZINC: a free tool to discover chemistry for biology. *J Chem Inf Model* **52,** 1757–1768 (2012).

150. Bussi, G. Hamiltonian replica exchange in GROMACS: a flexible implementation. *Molecular Physics* **112,** 379–384 (2014).
151. Wang, T., Marquardt, C. & Foker, J. Aerobic glycolysis during lymphocyte proliferation. *Nature* **261,** 702–705 (1976).
152. Parrinello, M. & Rahman, A. Polymorphic transitions in single crystals: A new molecular dynamics method. *Journal of Applied Physics* **52,** 7182–7190 (1981).
153. Hoover, W. Canonical dynamics: Equilibrium phase-space distributions. *Phys Rev A Gen Phys* **31,** 1695–1697 (1985).
154. Patriksson, A. & van der Spoel, D. A temperature predictor for parallel tempering simulations. *Phys Chem Chem Phys* **10,** 2073–2077 (2008).
155. Hess, B. P-LINCS: A Parallel Linear Constraint Solver for Molecular Simulation. *J Chem Theory Comput* **4,** 116–122 (2008).
156. Zeileis, A. & Grothendieck, G. zoo: S3Infrastructure for Regular and Irregular Time Series. *Journal of Statistical Software* **14,** 1–27 (2005).